nature cancer

Article

https://doi.org/10.1038/s43018-026-01259-3

Myeloid-derived TGFβ1 and oncostatin M establish two distinct stromal niches controlling late and hybrid EMT states

Received: 12 January 2026

Accepted: 21 September 2026

Check for updates

Anqi Dong[1,5], Sebastiaan Vanuytven[1,5], Andrea Pérez Gonzalez[1], Kevin Bevant[1], Lieselot Van de Putte[1], Zahra Zahedi[1], Justine Allard[2], Christine Dubois[1], Isabelle Salmon[3], Sandrine Rorive[3] & Cédric Blanpain[1,4]

Epithelial-to-mesenchymal transition (EMT) regulates tumor progression, metastasis and resistance to therapy. EMT encompasses a continuum of tumor states displaying different functions. The precise dialog between the tumor microenvironment and the different EMT states remains poorly understood. Using single-cell and spatial transcriptomics of mouse skin tumors, we uncover that different EMT states are associated with different niches. Neutrophils are more abundant in niches associated with hybrid EMT and secreted oncostatin M, which partially activates EMT while sustaining the epithelial program, promoting hybrid EMT states and metastasis formation. Macrophages are more abundant in niches associated with more advanced EMT states, which, together with other stromal cells, express TGFβ1 that promotes the late EMT state. Oncostatin M and TGFβ1 function in a feed-forward manner by creating distinct inflammatory niches to maintain specific EMT states. Together, our results reveal that distinct niches are associated with specific EMT states and that signaling pathways sustain their own niche's identity by recruiting specific myeloid cell populations.

Epithelial-to-mesenchymal transition (EMT) is a cellular process through which epithelial cells lose their epithelial characteristics and acquire mesenchymal features. EMT is associated with tumor progression, metastasis and therapy resistance[1–4]. Rather than a binary switch, EMT represents a continuum of distinct intermediate states exhibiting different functional properties[5–7]. Hybrid EMT states display the highest metastatic potential, fully mesenchymal states are more locally invasive, and both states contribute to therapy resistance. The transition between EMT states is tightly regulated by core EMT transcription factors (TFs) such as SNAI1 and ZEB1 that, together with additional TFs, maintain specific EMT states. Single-cell multiomic analysis and in situ characterization in mouse skin squamous cell carcinoma (SCC) identified four major EMT tumor states: an epithelial state (EpCAM$^+$KRT14$^+$vimentin$^-$), an early hybrid EMT state presenting a hybrid transcriptional program between epithelial and mesenchymal states (EpCAM$^-$KRT14$^+$vimentin$^+$), a more advanced hybrid EMT state (EpCAM$^-$KRT14$^-$KRT8$^+$vimentin$^+$) and a fully mesenchymal state (EpCAM$^-$KRT14$^-$KRT8$^-$vimentin$^+$)[2,8–10].

Cancer is a complex ecosystem in which tumor cells are embedded within a tumor microenvironment (TME) comprising different stromal cell types, including cancer-associated fibroblasts (CAFs), immune cells (such as macrophages, neutrophils and T cells), endothelial cells and pericytes[11–14]. These different stromal cells release a series of niche signals that shape cancer cell states and behaviors, including proliferation, invasion and EMT[15,16].

Tumor cells with different degrees of EMT are known to reside in inflammatory niches composed of monocytes, macrophages and CD8$^+$/CD4$^+$

[1]Laboratory of Stem Cells and Cancer, Université Libre de Bruxelles, Brussels, Belgium. [2]DIAPath, Center for Microscopy and Molecular Imaging, Université Libre de Bruxelles, Jumet, Belgium. [3]Centre Universitaire Inter Regional d'Expertise en Anatomie Pathologique Hospitalière (CurePath), CHIREC, CHU Tivoli and Université Libre de Bruxelles, Charleroi, Belgium. [4]WEL Research Institute, Université Libre de Bruxelles, Bruxelles, Belgium. [5]These authors contributed equally: Anqi Dong, Sebastiaan Vanuytven. e-mail: cedric.blanpain@ulb.be

T cells[5,7,17], associated with a highly vascularized environment[5,18]. These stromal cells are thought to communicate with tumor cells through the secretion of ligands that promote EMT[3]. Transforming growth factor-β (TGFβ), secreted by CAFs[19,20], macrophages[21,22] and endothelial cells[23], represents one of the best-characterized EMT-inducing signals. Additional cytokines and chemokines, including interleukin-6 (IL-6)[24,25], TNF[22] and CXCL12 (ref. 26), produced by activated T cells, CAFs and macrophages, have also been implicated in regulating EMT. Among these cytokines, the IL-6 family cytokine oncostatin M (OSM), has been shown to promote EMT and induce a stem cell-like feature in breast and pancreatic cancer cells[27–29]. Macrophage-derived OSM can induce a mesenchymal-like state in glioblastoma[30] and an inflammatory phenotype in the CAF population to support tumor growth and metastasis in pancreatic cancer[31]. However, it remains unclear how distinct inflammatory signals are spatially organized within the TME, whether they preferentially associate with specific EMT states and how they collectively regulate EMT progression. What are the key molecular pathways that regulate the communications between the various stromal cells and the different EMT states, and what are the specific extrinsic signals that induce and maintain each EMT state?

Here, using single-cell RNA sequencing (scRNA-seq) and spatial transcriptomics, we map the cellular composition and signaling architecture of the TME across different EMT states in mouse skin SCC. Our analyses reveal that EMT progression correlates with a shift from neutrophil-enriched niches surrounding the early EMT stages to macrophage-enriched niches around the later EMT states. We identify OSM and TGFβ1 as key extrinsic mediators creating these distinct inflammatory niches that maintain hybrid and late EMT states, respectively. These findings establish that EMT states are actively stabilized through state-specific extrinsic signals from spatially organized stromal niches, providing a framework for therapeutic targeting of distinct tumor cell states.

Results

Different stromal niches in skin SCC during EMT progression

To unravel how the TME composition changes with EMT, we performed scRNA-seq on mouse (*Lgr5*^{creER}; *Kras*^{G12D}; *Trp53*^{cKO}; *Rosa*-YFP (LKPR)) skin SCC cells sorted by fluorescence-activated cell sorting (FACS), presenting EMT. Across ten tumors with different degrees of EMT defined by the percentage of EpCAM$^+$ tumor cells, we defined the composition of the stromal cells associated with epithelial (n = 2, >90% EpCAM), mixed (n = 3, 10% < EpCAM < 90%) and mesenchymal tumors (n = 5, <10% EpCAM; Fig. 1a–c, Extended Data Fig. 1a–d and Supplementary Table 1).

The most abundant stromal cell populations across all tumors were myeloid cells (macrophages and neutrophils) and CAFs (Fig. 1b,d). Tumor cells were identified by yellow fluorescent protein (YFP) transgene expression and the presence of copy number aberrations inferred by inferCNV[32] (Extended Data Fig. 1c,d). Within the CD45$^+$CD31$^+$ (Lin$^+$) compartment, macrophages were enriched in mesenchymal tumors, whereas neutrophils were enriched in epithelial and mixed tumors (scCODA, all false discovery rate (FDR) < 0.1; Fig. 1d).

Subclustering of CAFs, macrophages and neutrophils revealed further heterogeneity (Fig. 1e–h). CAFs comprised myofibroblastic CAFs, inflammatory CAFs and *Wif1*$^+$ CAFs resembling skin papillary fibroblasts[33,34] (Fig. 1e and Extended Data Fig. 1f). As previously described, macrophage subclustering identified four tumor-associated macrophages (TAMs): *Cxcl9*$^+$, *Il1b*$^+$, *Spp1*$^+$ and *Folr2*$^+$[35], alongside *Cd14*$^+$ and *Irf7*$^+$ monocytes, and a new *Ctsk*$^+$ TAM population that was differentially enriched in tumors with different degrees of EMT (Fig. 1f and Extended Data Fig. 1g). T cell subclustering identified CD4$^+$ T, CD8$^+$ T, γδ T, T helper 17 and regulatory T cell subsets as well as natural killer cells, with no significant relative abundance across tumor types (Fig. 1g and Extended Data Fig. 1h). Neutrophils formed five clusters (*Ctsb*$^+$, *Isg15*$^+$, *Mpp7*$^+$, *Retnlg*$^+$ and *Tnf*$^+$), reflecting distinct functional states[36], with similar proportions across tumor types (Fig. 1h and Extended Data Fig. 1i).

In summary, tumors with different EMT phenotypes harbor distinct TMEs, with neutrophils and CAFs dominating epithelial tumors and macrophages and T cells more abundant in mesenchymal tumors.

Spatial transcriptomics reveal distinct EMT niches

To investigate the spatial organization of these EMT-associated TME compositions, we performed 10x Xenium spatial transcriptomics on one epithelial, two mixed and two mesenchymal tumors. Alongside tumor cells, we identified diverse stromal and immune populations including CAFs, macrophages, neutrophils and T cells (Fig. 2a and Extended Data Fig. 2a).

TME composition differed markedly by tumor type. Epithelial/mixed tumors contained more CAFs and neutrophils, while macrophages, mast cells and vascular endothelial cells (VECs) were enriched in mesenchymal tumors (Fig. 2b). Architecturally, epithelial and mixed SCCs showed dense tumor trabeculae intermingled with stromal cells, whereas mesenchymal tumors had minimal organized stroma with dense macrophage/VEC infiltration. In epithelial/mixed tumors, CAFs colocalized with macrophages and VECs, away from neutrophils, whereas in mesenchymal tumors, CAFs were restricted to the tumor border without macrophage colocalization (Fig. 2c). Subclustering of CAFs, macrophages, neutrophils and T cells largely recapitulated scRNA-seq-derived states, often with an additional proliferating cluster (Extended Data Fig. 2b–e).

To validate these findings in a larger cohort of tumors, we performed in situ immunofluorescence staining of neutrophils (Ly6G$^+$), macrophages (F4/80$^+$), CAFs (ACTA2$^+$), T cells (CD3$^+$), endothelial cells (CD31$^+$), lymphatic endothelial cells (LECs; PROX1$^+$) and pericytes (DES$^+$) across 15 tumors (5 epithelial, 5 mixed and 5 mesenchymal), confirming the spatial transcriptomics results: CAFs and neutrophils were enriched in mixed tumors, whereas macrophages, LECs, VECs, pericytes and T cells were enriched in mesenchymal tumors, recapitulating key spatial patterns, including tumor-adjacent neutrophil localization in mixed tumors and CAF peripheral localization in mesenchymal tumors (Extended Data Fig. 2f).

Together, these data reveal that TME composition shifts with the degree of EMT and is coupled with distinct spatial architectures.

Neutrophil and macrophage niches with distinct EMT states

In our scRNA-seq dataset, subclustering of tumor cells identified the four previously described states: epithelial, early hybrid, hybrid and late EMT (Extended Data Fig. 3a,b). Metabolic profiling showed

Fig. 1 | Identification of distinct TME stromal cells in skin SCC by scRNA-seq. **a**,**b**, Uniform manifold approximation and projection (UMAP) of integrated single-cell transcriptomic data from 10 primary skin SCCs exhibiting varying degrees of EMT, colored by inferred cell type in the combined dataset (10 tumors, 39,612 cells; **a**) and split by tumor type (2 epithelial tumors, 8,902 cells; 3 mixed tumors, 14,052 cells; 5 mesenchymal tumors, 16,658 cells; **b**). **c**, Heat map showing *z*-scored expression of the top three differentially expressed genes for each TME cell type across ten SCC tumors. Rows (genes) are ordered by hierarchical clustering using Ward's D2 method. **d**, Box plot depicting the proportion of each TME cell type within Lin$^+$ and Lin$^-$ stromal populations across individual tumors. Asterisks indicate significant differential abundance (FDR < 0.1, scCODA analysis). Box plots are colored by tumor type; n = 2, 3 and 5 tumors for epithelial, mixed and mesenchymal tumor types, respectively. The center line represents the median, box edges delineate the 25th and 75th percentiles, and whiskers extend to 1.5 times the interquartile range (IQR). **e**–**h**, UMAP plots depicting transcriptomic subclusters identified across the 10 SCC tumors within CAFs (4,437 cells; **e**), macrophages (3,829 cells; **f**), T cells (932 cells; **g**) and neutrophils (10,905 cells; **h**), colored by inferred subpopulation identity; iCAF, inflammatory CAFs; myCAF, myofibroblastic CAFs; NK, natural killer; T_H17 cells, IL-17-producing helper T cells; T_{reg} cells, regulatory T cells.

https://doi.org/10.1038/s43018-026-01259-3

minimal differences across states at the single-cell level (Extended Data Fig. 3c). Xenium transcriptomics also identified the four EMT states: epithelial (*Epcam*$^+$, *Ovol1*$^+$, *Cdh1*$^+$, *Trp63*$^+$), early hybrid (*Epcam*$^-$, *Pitx1*$^+$, *Klf5*$^+$, *Trp63*$^+$), hybrid (*Cdh2*$^+$, *Zeb1*$^+$, *Twist1*$^+$, *Pdgfra/Pdgfrb*$^-$, *Postn*$^-$) and late EMT (*Zeb1*$^+$, *Pdgfra/Pdgfrb*$^+$, *Postn*$^+$, *Col1a1*$^+$; Fig. 3a–d). Epithelial and early hybrid EMT states predominated in epithelial/mixed SCCs, whereas hybrid and late EMT states were enriched in mesenchymal tumors (Figs. 2c and 3e). In mixed tumors, epithelial and early hybrid

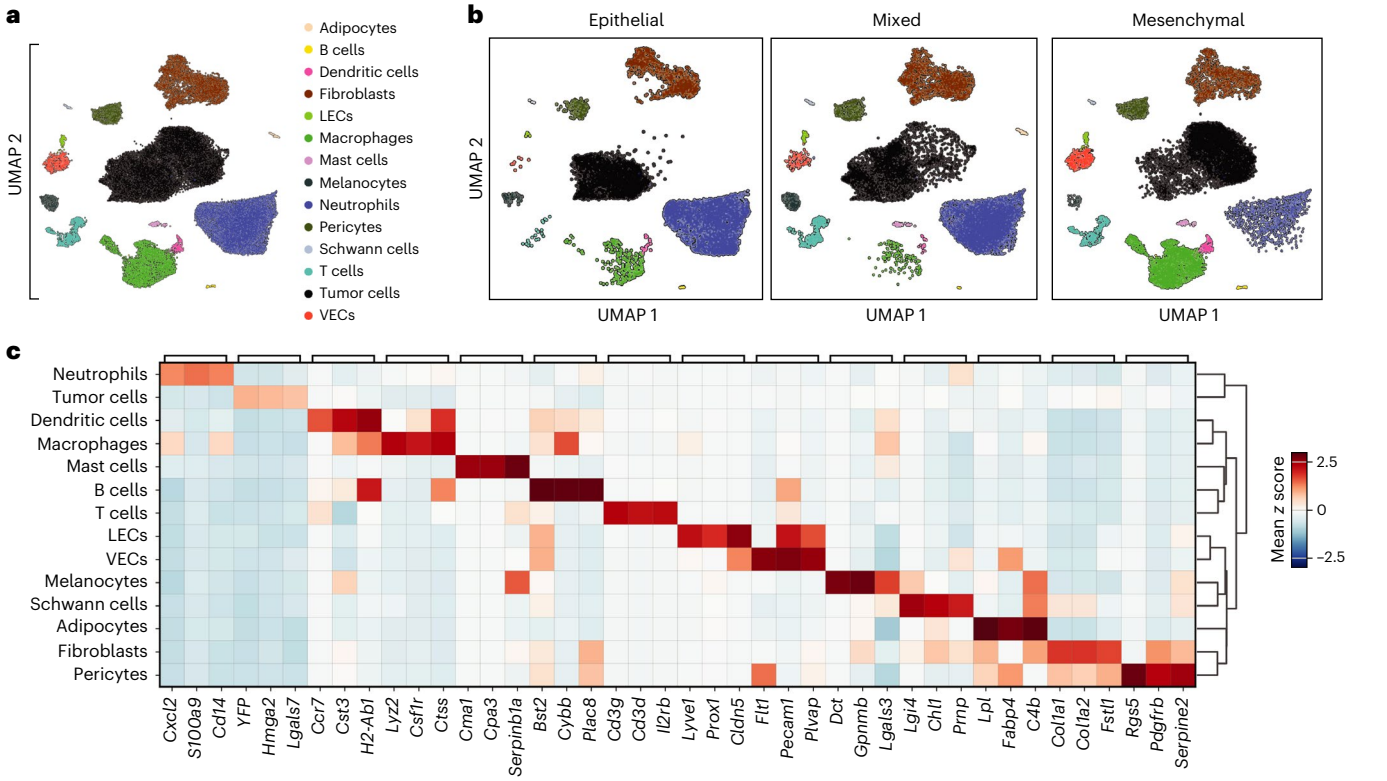

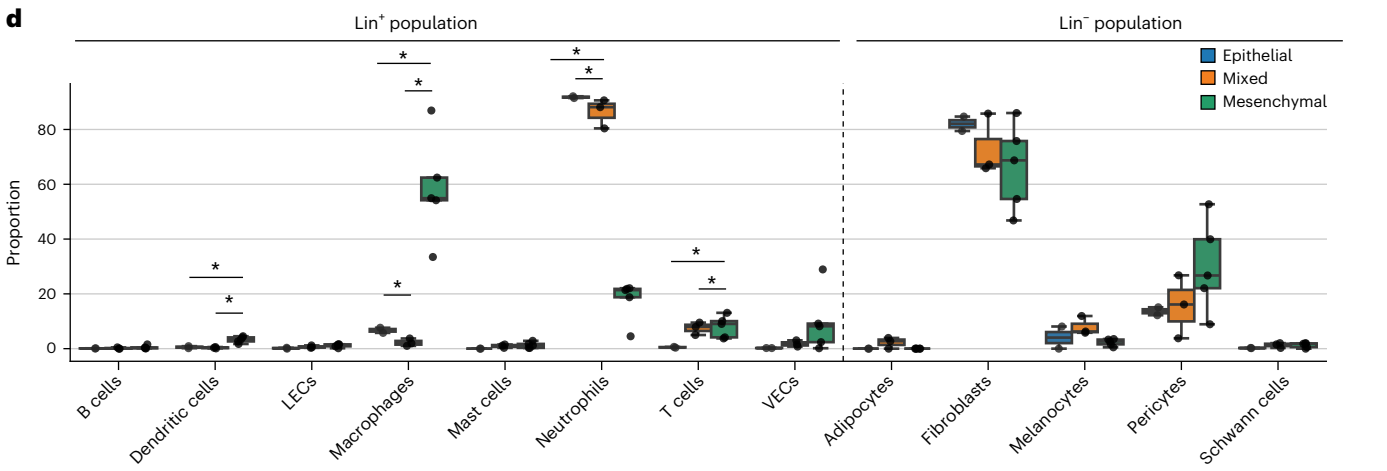

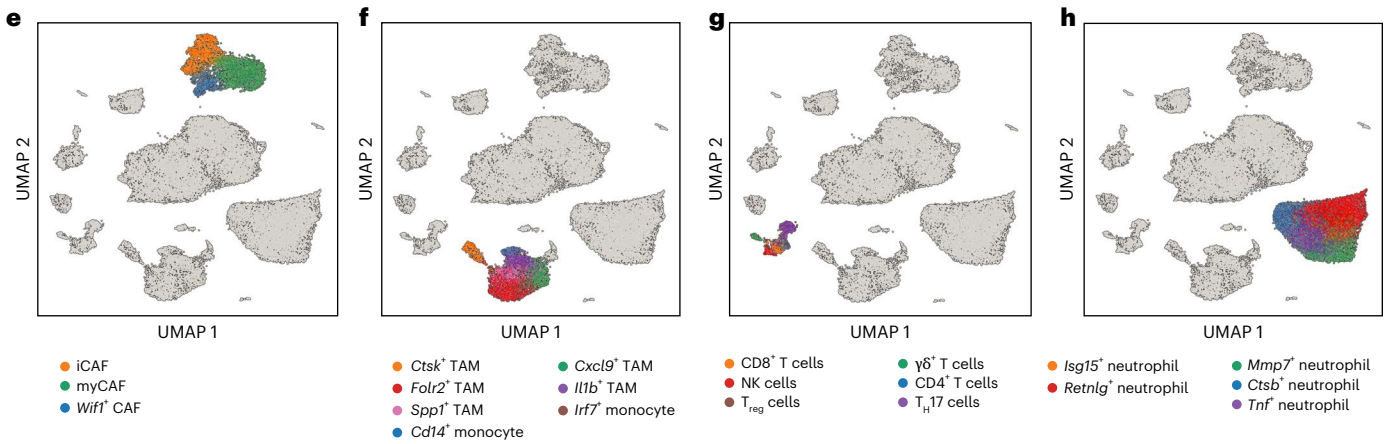

https://doi.org/10.1038/s43018-026-01259-3

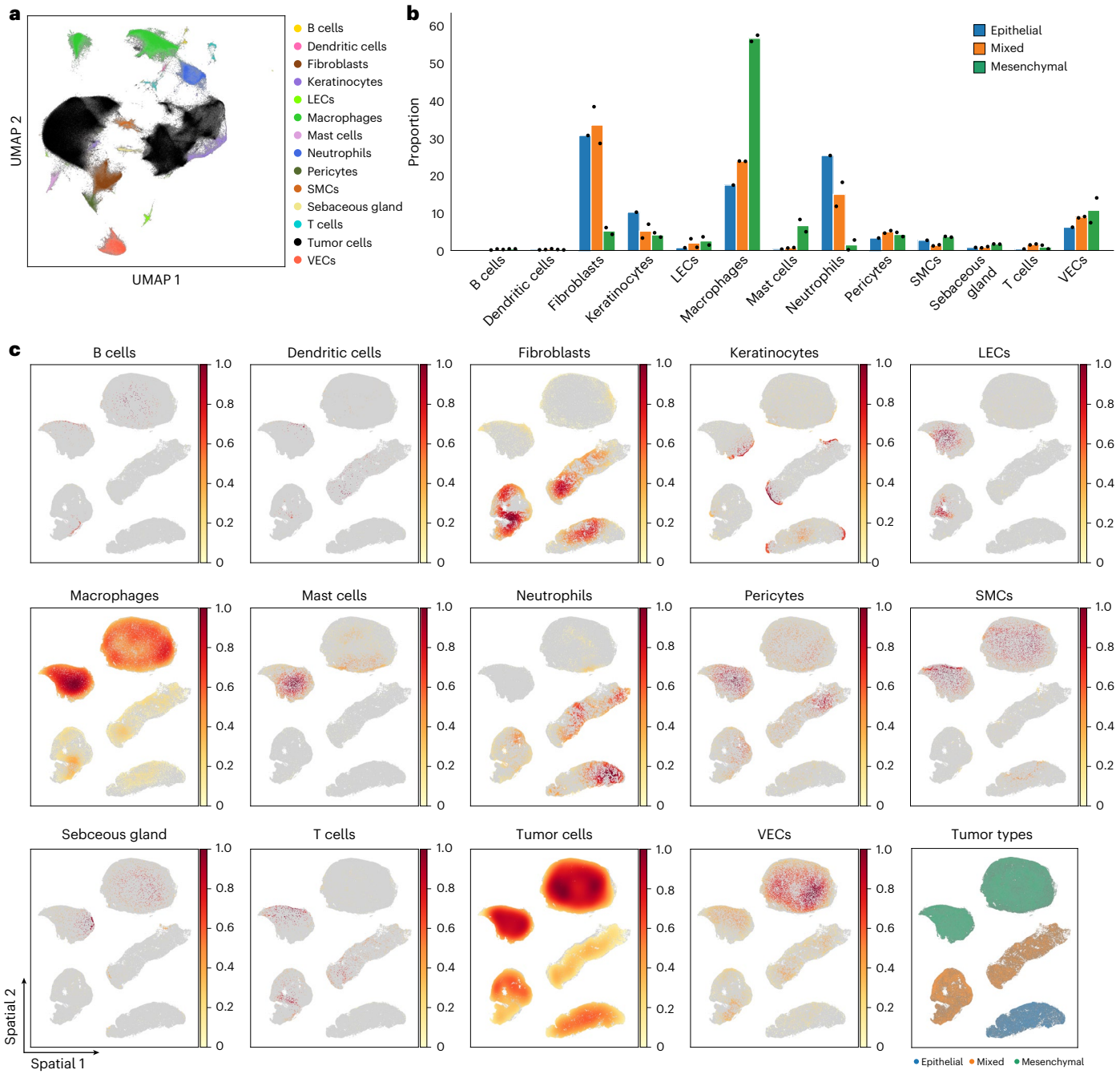

Fig. 2 | Spatial transcriptomic profiling reveals distinct cellular niches in mixed and mesenchymal skin SCCs. a, UMAP plot of cells from the Xenium spatial transcriptomics dataset that passed quality control, colored by cell type. Each dot represents a cell (5 tumors, 749,577 cells); SMCs, smooth muscle cells. **b**, Bar plot depicting the composition of nontumor cells within each TME cell type (tumor cells included) across individual tumors. Bars are colored by tumor type, with dots representing individual tumors; $n = 1, 2$ and 2 tumors for epithelial, mixed and mesenchymal tumor types, respectively. **c**, Density plots showing the spatial distribution of individual cell types in individual tumors. The color scale indicates the density of the specified cell type, while cells not belonging to that cell type are shown in gray. The bottom-right image is colored by tumor classification based on EpCAM$^+$ percentage of tumor cells: epithelial (109,326 cells), mixed (203,105 cells) and mesenchymal (437,146 cells).

EMT states occupied spatially distinct regions, both showing the presence of CAFs and neutrophils. In addition, the epithelial state niche contained macrophages, whereas the early hybrid niche was enriched for VECs, LECs and pericytes. In mesenchymal tumors, the hybrid EMT state was distributed throughout the tumor while the late EMT state was enriched at the border, both sharing a macrophage/mast cell/smooth muscle cell-rich niche (Fig. 3f–i).

Niche enrichment analysis (60-µm radius, *z*-scored TME abundances) confirmed these EMT state-specific compositions: epithelial and early hybrid niches were enriched for CAFs and neutrophils with low abundance of macrophages, whereas hybrid and late EMT niches were enriched for macrophages with low neutrophil/CAF infiltration. Pericytes, LECs, mast cells and VECs showed additional state-specific enrichment patterns (Extended Data Fig. 3d). Despite reduced CAF abundance, late EMT tumors retained strong collagen deposition, suggesting that tumor cells themselves contribute to extracellular matrix (ECM) deposition at this stage (Extended Data Fig. 3e).

https://doi.org/10.1038/s43018-026-01259-3

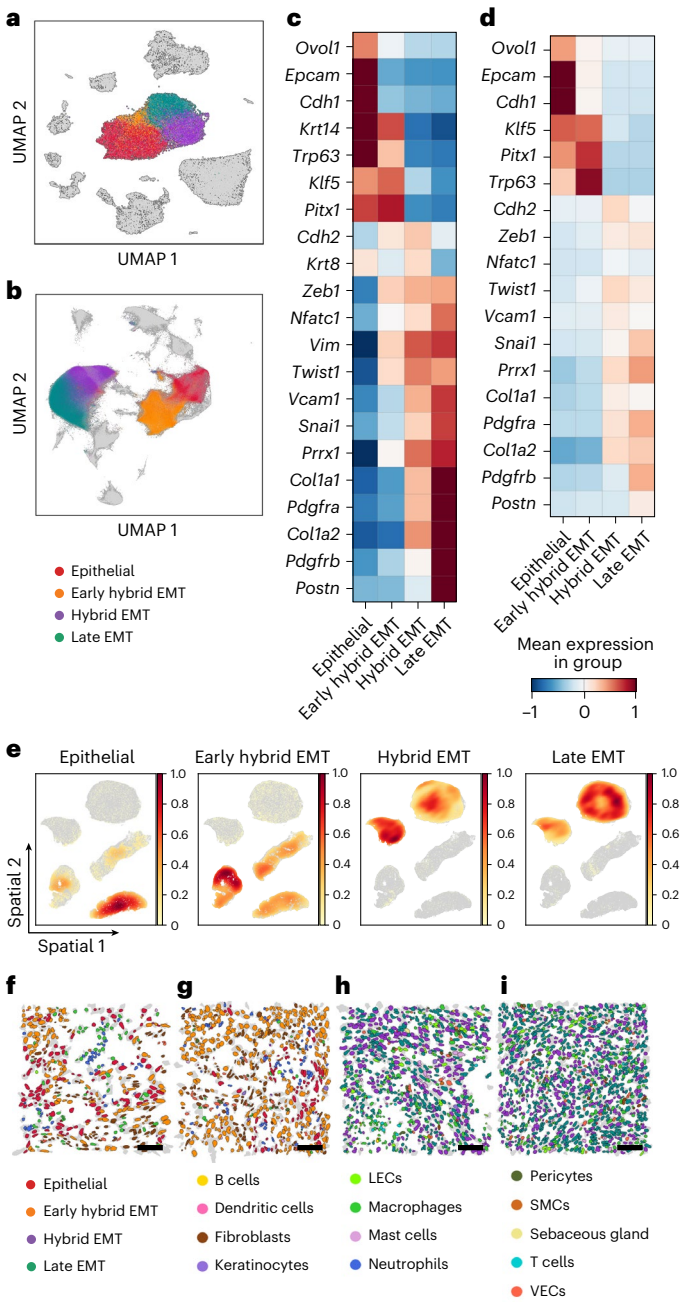

Fig. 3 | Identification of distinct niches associated with different EMT states. a,**b**, UMAP plots of tumor cells from the integrated scRNA-seq dataset (10 tumors, 16,708 cells; **a**) and the Xenium spatial transcriptomics dataset (5 tumors, 540,478 cells; **b**). Cells are colored by inferred EMT states; nontumor cells are shown in gray. **c**,**d**, Heat maps displaying scaled expression of canonical EMT-related genes across EMT states in the integrated scRNA-seq dataset (**c**) and the spatial transcriptomics dataset (**d**). **e**, Density maps showing the spatial distribution of the four EMT states in individual tumors. The color scale indicates the density of the specified EMT state, while cells not belonging to that state are shown in gray. The numbers of cells assigned to the epithelial, early hybrid EMT, hybrid EMT and late EMT states are 71,631, 147,593, 143,887 and 177,367, respectively. **f**–**i**, Spatial organization of EMT states and TME components in 300-µm regions enriched for tumor cells in the epithelial (**f**), early hybrid EMT (**g**), hybrid EMT (**h**) and late EMT (**i**) states. Cell boundaries are displayed in gray; nuclei are colored by EMT state or TME component identity; scale bars, 50 µm.

Subcluster-level analysis further refined these compositional patterns, showing that individual CAF, macrophage, T cell and neutrophil subsets followed distinct, state-specific distributions across the epithelial-to-late EMT trajectory (Extended Data Fig. 3f–j).

Immunostaining validation across a larger cohort (five tumors per state) confirmed this spatial architecture. Neutrophils peaked in early hybrid EMT and declined thereafter. CAFs were most abundant in the early hybrid EMT state. Macrophages, endothelial cells, LECs and T cells progressively increased toward late EMT (Fig. 4a–g).

Together, these data show that EMT progression is accompanied by coordinated TME remodeling: epithelial niches are CAF-rich with diverse immune populations, early hybrid niches are rich in neutrophils, and hybrid niches show increased macrophage and vascular infiltration, whereas late EMT niches are composed of macrophages, T cells and VECs with reduced CAFs and neutrophils.

Neutrophil and macrophage depletion impairs EMT-specific niches

To determine the role of neutrophil and macrophage niches in the regulation of EMT states and metastatic potential, we depleted neutrophils (anti-Ly6G) or macrophages (blocking antibodies to CSF1R and CCL2) in transplanted primary skin SCCs (Extended Data Fig. 4a,b). Neutrophil depletion reduced the hybrid EMT state and increased the late EMT state, while macrophage depletion decreased EMT progression overall as previously reported[5] (Fig. 4h). Neutrophil depletion increased macrophage abundance within the small remaining hybrid EMT population (Extended Data Fig. 4c–e), whereas macrophage depletion increased neutrophil infiltration, particularly in early hybrid EMT regions (Extended Data Fig. 4f–h), suggesting cross-regulation between the different myeloid populations across EMT-associated niches. Neutrophil depletion also reduced lung metastasis (Fig. 4i,j and Extended Data Fig. 4i–k), consistent with the established high metastatic potential of hybrid EMT states[5–7,37].

These findings provide functional evidence that myeloid composition actively regulates EMT states, with neutrophils required to maintain the hybrid EMT state, raising the question of which specific signals mediate this tumor–myeloid cross-talk.

Cell–cell communication between stromal and EMT tumor states

To identify ligand–receptor pairs mediating stromal–tumor communication across EMT states, we ran CellPhoneDB[38] and CellChat[39] per tumor ($n = 10$), combining interaction scores across samples with EMT states as receivers and prioritizing communication from the most abundant TME components: macrophages, neutrophils, T cells, CAFs, VECs, LECs and pericytes (Fig. 5a,b). Given our functional data on the impact of neutrophil/macrophage depletion on EMT dynamics (Fig. 4h), and their different abundance in epithelial/mixed and mesenchymal tumors (Fig. 1d), we focused on neutrophil-to-early hybrid EMT and macrophage-to-hybrid/late EMT tumor cell communication and identified 25 and 18 candidate ligand–receptor pairs shared between tools, respectively (Extended Data Fig. 5a–d). Pairs with biology incompatible with EMT promotion, with immunosuppressive or metabolic functions unrelated to EMT or lacking EMT-relevant literature support were excluded for functional analysis. This effort yielded four neutrophil-derived (TNF–TNFRSF1A/TNFRSF1B, IL-1A/IL-1B–IL-1R1/IL-1RAP, OSM–IL-6ST/OSMR/LIFR and TGM2–ADGRG1) and seven macrophage-derived (VEGFA–NRP1, OSM–IL-6ST/OSMR/LIFR, IL-1A/IL-1B–IL-1R1/IL-1RAP, SEMA4A–PLXND1, TNF–TNFRSF1A, TGFB1–TGFBR1/TGFBR2 and PDGF-B–PDGF-C) candidate ligands for in vitro functional screening. Q16

ScRNA-seq analysis revealed distinct cell-type specificities for each ligand (Extended Data Fig. 5e–g). *Tnf* and *Il1a*/*Il1b* were predominantly expressed by neutrophils/macrophages; *Osm* by neutrophils, macrophages and mast cells; *Tgm2* by neutrophils, macrophages, LECs and VECs; *Sema4a* by neutrophils, T cells, macrophages and a subset of tumor cells; *Vegfa* by tumor cells, neutrophils and macrophages; *Pdgfb* predominantly by VECs, macrophages and tumor cells; *Pdgfc* by tumor cells and CAFs and *Tgfb1* by nearly all TME components. All cognate receptors were expressed in tumor cells except *Il1r2*, with clear

https://doi.org/10.1038/s43018-026-01259-3

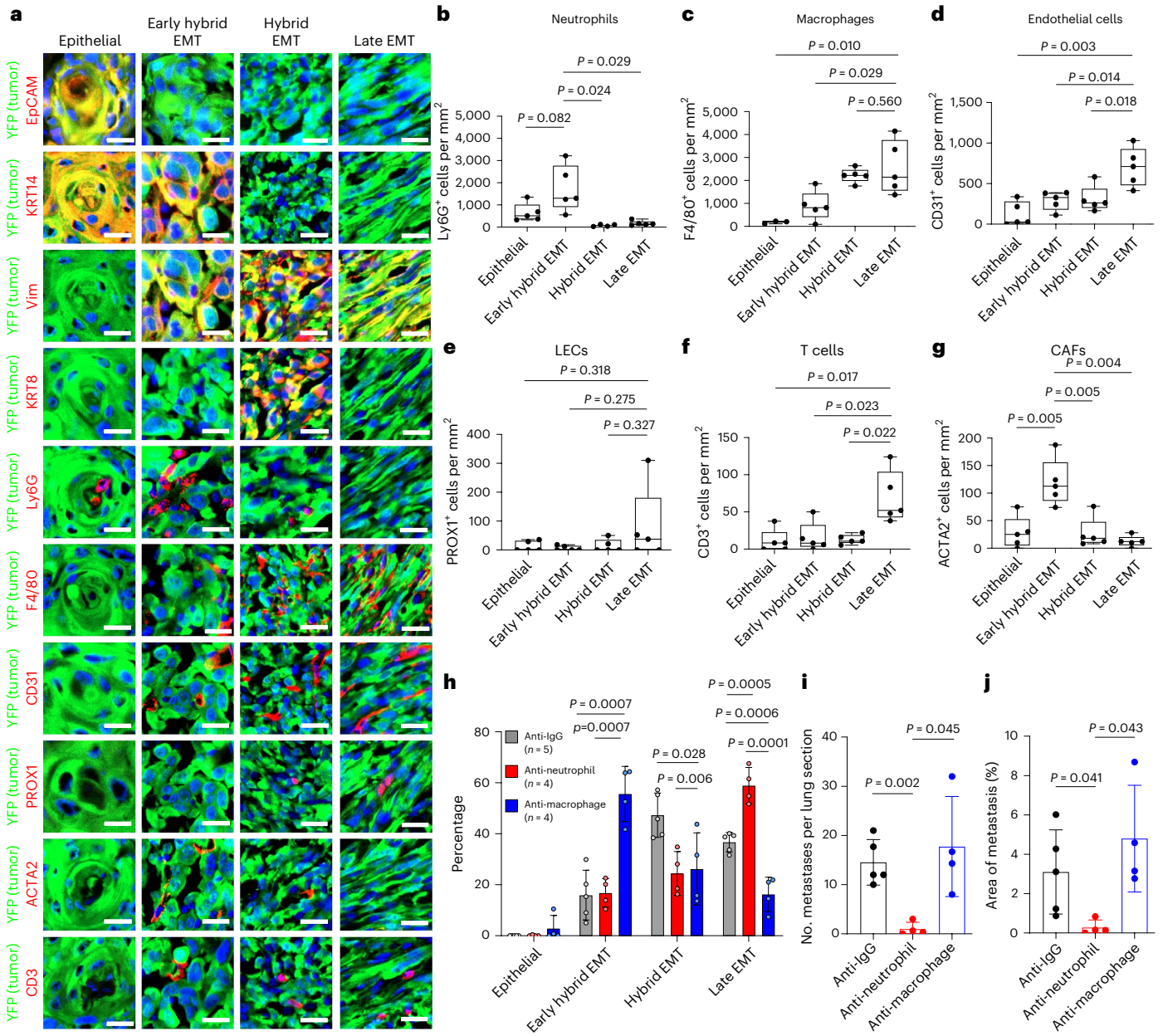

Fig. 4 | Neutrophils and macrophages regulate distinct EMT states. **a**, Immunofluorescence showing the presence of the major TME components in different EMT states; scale bars, 20 µm. Immunofluorescence was performed on sequential sections and as triple staining for YFP/vimentin/KRT14, YFP/vimentin/KRT8 and YFP/CD31/PROX1. Representative images are shown from five tumors per EMT state, with similar results obtained in each tumor; Vim, vimentin. **b**–**g**, Quantification of neutrophil (**b**), macrophage (**c**), endothelial cell (**d**), LEC (**e**), T cell (**f**) and CAF (**g**) abundance in different EMT states; $n = 5$ tumors analyzed for each TME component and EMT state. Box plots show the minimum to maximum range, with the horizontal line indicating the median. Data represent the mean ± s.d., analyzed using an unpaired two-sided *t*-test with Welch's correction. **h**, Cytospin immunostaining quantification of KRT14, KRT8 and vimentin from transplanted tumors following control treatment (anti-IgG, $n = 5$ mice, 1,421 cells analyzed), neutrophil depletion (anti-neutrophil, $n = 4$, 890 cells analyzed) or macrophage depletion (anti-macrophage, $n = 4$, 857 cells analyzed). Data represent the mean ± s.d., analyzed using multiple *t*-tests. **i**,**j**, Quantification of the number (**i**) and area (**j**) of lung metastases in mice with transplanted tumors following anti-IgG ($n = 5$ mice), anti-neutrophil ($n = 4$ mice) and anti-macrophage ($n = 4$ mice) treatment. Data represent the mean ± s.d., analyzed using an unpaired two-sided *t*-test with Welch's correction.

EMT state-specific enrichment; *Adgrg1* in epithelial and early hybrid states; *Lifr* and *Osmr* from early hybrid to late EMT; *Tgfbr1*/*Tgfbr2* across all states, peaking in late EMT, and *Pdgfra*, *Pdgfrb*, *Il6st* and *Nrp1* in the late EMT state (Extended Data Fig. 5h).

All selected ligands except *Il1b* and *Pdgfc* were present in the Xenium 5K panel and showed high expression in macrophages across tumor types (except for *Vegfa*), and receptors were detected in good agreement with the scRNA-seq data (Fig. 5c–f and Extended Data Fig. 5i,j). Ligand and receptor interaction analysis in spatial transcriptomics (LARIS)-based spatial ligand–receptor analysis validated seven of ten ligands (Extended Data Fig. 5k), with OSM signaling predominantly from neutrophils to all EMT states, TGFβ1 from macrophages, neutrophils and dendritic and B cells to the late EMT niche and the remaining pairs (TNF, TGM2, PDGF-B) showing state- and source-specific patterns (Extended Data Fig. 5l).

To assess the function of these ligand–receptor interactions in the regulation of EMT, we treated epithelial tumor cells in vitro with recombinant proteins and monitored EpCAM expression over time.

TGFβ1, OSM and TNF emerged as potent EMT inducers, whereas IL-1β, PDGF-AB, SEMA4A, TGM2 and VEGF showed no effect (Fig. 5g,h). TGFβ1 and TNF are known to promote EMT through the upregulation of EMT TFs SNAIL, ZEB1 and TWIST[40–43], and macrophage-derived OSM has been linked to mesenchymal transition in glioblastoma[30] and cooperates with TGFβ–SMAD signaling to promote EMT in human mammary epithelial cells[29]. However, the specific EMT state promoted by OSM and whether it differs from TGFβ1-induced EMT remains unclear.

We next examined the myeloid cellular sources of these ligands. *Tnf* and *Tgfb1* were coexpressed by *Tnf*$^+$ and *Isg15*$^+$ neutrophils (epithelial niche-associated), while *Osm* was expressed by *Retnlg*$^+$ neutrophils (enriched in the early hybrid EMT niche; Extended Data Figs. 3j and 5f). Among macrophages, *Tnf* was mainly expressed by *Cxcl9*$^+$ TAMs and *Irf7*$^+$ monocytes, *Osm* by *Il1b*$^+$ TAMs and *Cd14*$^+$ monocytes and *Tgfb1* broadly across all TAM/monocyte subsets (Extended Data Fig. 5g).

In situ RNAscope confirmed these expression patterns. *Osm* transcripts were detected in macrophages and neutrophils within early hybrid and hybrid EMT tumors, while *Tgfb1* was expressed broadly by stromal cells across all EMT state niches (Fig. 5i–m). Notably, neutrophils were the predominant *Osm* source in early hybrid EMT tumors, while macrophages became the principal source of *Osm* within hybrid EMT tumors (Fig. 5i–l).

Together, these data show that although both TGFβ1 and OSM promote EMT, they are secreted by distinct TME populations with different spatial distributions. OSM is restricted to myeloid populations enriched in early hybrid and hybrid EMT states, while TGFβ1 has a broader cellular source spanning across all EMT states.

EMT states express distinct myeloid cell chemoattractants

Using the same bioinformatic approach, we identified ligand–receptor pairs mediating neutrophil and macrophage recruitment by different EMT states, yielding 77 pairs detected by both tools (Extended Data Fig. 6a). Neutrophil recruitment was predominantly dominated by CSF3–CSF3R[44] and multiple CXCR2-binding chemokines (CXCL1/CXCL2/CXCL3/CXCL5/CXCL6), the primary neutrophil chemoattractant axis[45]. Macrophage recruitment was predominantly mediated by CCL2–CCR2 (ref. 46), with additional contributions from CSF1/IL-34–CSF1R[47], CCL7–CCR1/CCR2 (ref. 48) and CX3CL1–CX3CR1 (ref. 49).

LARIS analysis of spatial transcriptomic data confirmed the ligand–receptor pairs associated with the chemoattraction of macrophages, with CCL2–CCR2, CCL7–CCR1/CCR2 and CX3CL1–CX3CR1 signaling starting in the early hybrid EMT state and the latter increasing in the hybrid and late EMT states (Extended Data Fig. 6b). IL-34–CSF1R and CSF1–CSF1R signaling in the hybrid and late EMT states, respectively, support M2 polarization and TAM survival. For neutrophil recruitment and expansion, CSF3–CSF3R signaling was found in epithelial and early hybrid EMT states and CXCL1–CXCR2 in the early hybrid state.

OSM sustains hybrid EMT whereas TGFβ1 promotes late EMT

To investigate whether TGFβ1 and OSM drive different EMT states, we treated FACS-isolated EpCAM$^+$ tumor cells with recombinant TGFβ1 or OSM in vitro and tracked EMT phenotype over time (Fig. 6a). OSM induced a rapid, binary shift in EpCAM expression by day 7, whereas TGFβ1 produced a more gradual decline of EpCAM expression (Extended Data Fig. 7a). Cytospin analysis using state-specific makers showed that by day 7, TGFβ1-treated cells were already more advanced toward the hybrid EMT state (20%) than OSM-treated cells (8%), which remained predominantly in the epithelial state (46%; Extended Data Fig. 7b). By day 13, most TGFβ1-treated cells expressed vimentin, with a subset reaching the late EMT state (14%), whereas OSM-treated cells remained largely epithelial (43%) or early hybrid/hybrid (Fig. 6b). Consistently, in vivo co-transplantation of tumor cells with doxycycline-inducible *Osm*- or *Tgfb1*-overexpressing macrophages (versus empty vector controls) showed that *Osm* overexpression increased early hybrid EMT state and neutrophil infiltration, whereas *Tgfb1* overexpression increased late EMT cells (Extended Data Fig. 7c,d), confirming that stromal-derived OSM and TGFβ1 promote distinct EMT states and niche organization in vivo.

OSM and TGFβ1 induce STAT3 and SMAD2/SMAD3 phosphorylation, respectively[50,51] (Extended Data Fig. 7e,f). Immunohistochemistry showed pSTAT3 activation preferentially in early hybrid and hybrid EMT states, with neutrophils significantly enriched near pSTAT3^{hi} regions in the early hybrid EMT state, whereas pSMAD2 was detected across all EMT states (Fig. 6c,d). JAK inhibition (ruxolitinib) blocked STAT3 phosphorylation and the OSM-induced epithelial-to-hybrid EMT transition (Fig. 6e and Extended Data Fig. 7e). By contrast, TGFBR inhibition (SB431542) blocked TGFβ1-induced EMT (Fig. 6f and Extended Data Fig. 7f). Similarly, CRISPR knockout of *Osmr* or *Tgfbr2* blocked EMT following OSM or TGFβ1 treatment, respectively (Extended Data Fig. 7g–j).

To investigate the cross-talk between the two pathways, we co-treated cells with OSM and SB431542, which led to reduced progression to the hybrid EMT state (Fig. 6f). OSM treatment of *Tgfbr2*-knockout cells impaired progression from the early hybrid to hybrid EMT state (Extended Data Fig. 7j), consistent with a previous report showing that inhibition of the TGFβ receptor blocks OSM-induced EMT in human mammary epithelial cells[29]. Conversely, TGFβ1 treatment with OSM signaling blockade using either JAK–STAT inhibition or *Osmr* knockout did not affect TGFβ1-induced progression to late EMT (Fig. 6e and Extended Data Fig. 7i).

Together, these data show that OSM and TGFβ1 promote the hybrid and late EMT states, respectively. TGFβ1-mediated EMT is independent of OSM signaling, whereas OSM-induced EMT partially depends on TGFBR activity.

OSM and TGFβ1 regulate different EMT states

To dissect the molecular mechanisms underlying TGFβ1- and OSM-induced EMT, we treated EpCAM$^+$ tumor cells with recombinant TGFβ1 or OSM in vitro, isolated EpCAM^{hi}, EpCAM^{mid} and EpCAM^{neg} populations at day 13 using FACS and performed bulk RNA-seq (Fig. 7a and Extended Data Fig. 7a). Cytospin analysis confirmed that TGFβ1-treated cells reached a later EMT state than OSM-treated cells across all EpCAM populations

Fig. 5 | Identification and validation of EMT-promoting ligands from the TME. a,**b**, Interaction maps showing significant ligand–receptor interactions from major TME cell types to tumor cells across EMT states, identified using CellPhoneDB (**a**) and CellChat (**b**); $n = 10$ tumors. Node and edge colors indicate cell type; edge thickness indicates interaction numbers. **c**–**f**, Heat maps depicting *z*-scaled expression of identified ligands in epithelial (**c**), mixed (**d**) and mesenchymal (**e**) tumors and corresponding receptors in EMT states (**f**) in the spatial transcriptomics dataset; $n = 5$ tumors. **g**, Flow cytometry analysis of EpCAM percentage in mouse skin SCC-derived cells after 7 days of treatment with the indicated recombinant proteins (50 ng ml^{-1}); $n = 3$ independent experiments for control, TNF, TGFβ1 and OSM; $n = 2$ independent experiments for the other conditions. Data represent the mean ± s.d.; Ctrl, control. **h**, Time course analysis of EpCAM expression following treatment with the indicated recombinant proteins ($n = 3$ independent experiments per condition). Data represent the mean ± s.d., analyzed using a two-sided unpaired *t*-test with Welch's correction; D, day. **i**–**l**, Quantification of *Osm*$^+$ cell number (**i** and **j**) and proportion (**k** and **l**) per ×60 field of view in early hybrid (**i** and **k**) and hybrid EMT states (**j** and **l**). Data comprise 13 and 10 images from three tumors for neutrophils and macrophages, respectively, in early hybrid regions and 9 and 13 images from three tumors for neutrophils and macrophages, respectively, in hybrid EMT regions. Data represent the mean ± s.d., analyzed using a two-sided unpaired *t*-test with Welch's correction. For box plots, the center line represents the median; NS, not significant. **m**, Immunofluorescence and RNAscope analysis showing the spatial localization of *Osm*- and *Tgfb1*-expressing macrophages and neutrophils in tumor regions with distinct EMT states; scale bars, 10 µm. Immunofluorescence was performed in sequential sections with triple staining for YFP/vimentin/KRT14 and YFP/vimentin/KRT8. Representative images are shown from three tumors per EMT state, with similar results obtained in each tumor.

https://doi.org/10.1038/s43018-026-01259-3

(Extended Data Fig. 8a). Principal component analysis (PCA) showed that OSM- and TGFβ1-treated tumor cells present different distinct transcriptomic states. TGFβ1 induced a progressive shift along principal component 1 (PC1), which is associated with EMT, whereas OSM shifted cells along PC2, which is associated with hypoxia and inflammation, including TNF and interferon-γ pathways (Fig. 7a and Extended Data Fig. 8b–e).

Although both OSM and TGFβ1 downregulated the expression of classical epithelial genes (*Epcam*, *Cdh1* and *Irf6*) and upregulated the expression of common mesenchymal genes (*Vim*, *Cdh2* and *Fn1*; Fig. 7b), they induced distinct transcriptional programs (Fig. 7c–g and Extended Data Fig. 8f). TGFβ1 induced *Zeb1* expression more strongly, whereas OSM induced *Snai1* and *Klf5* expression. OSM additionally upregulated

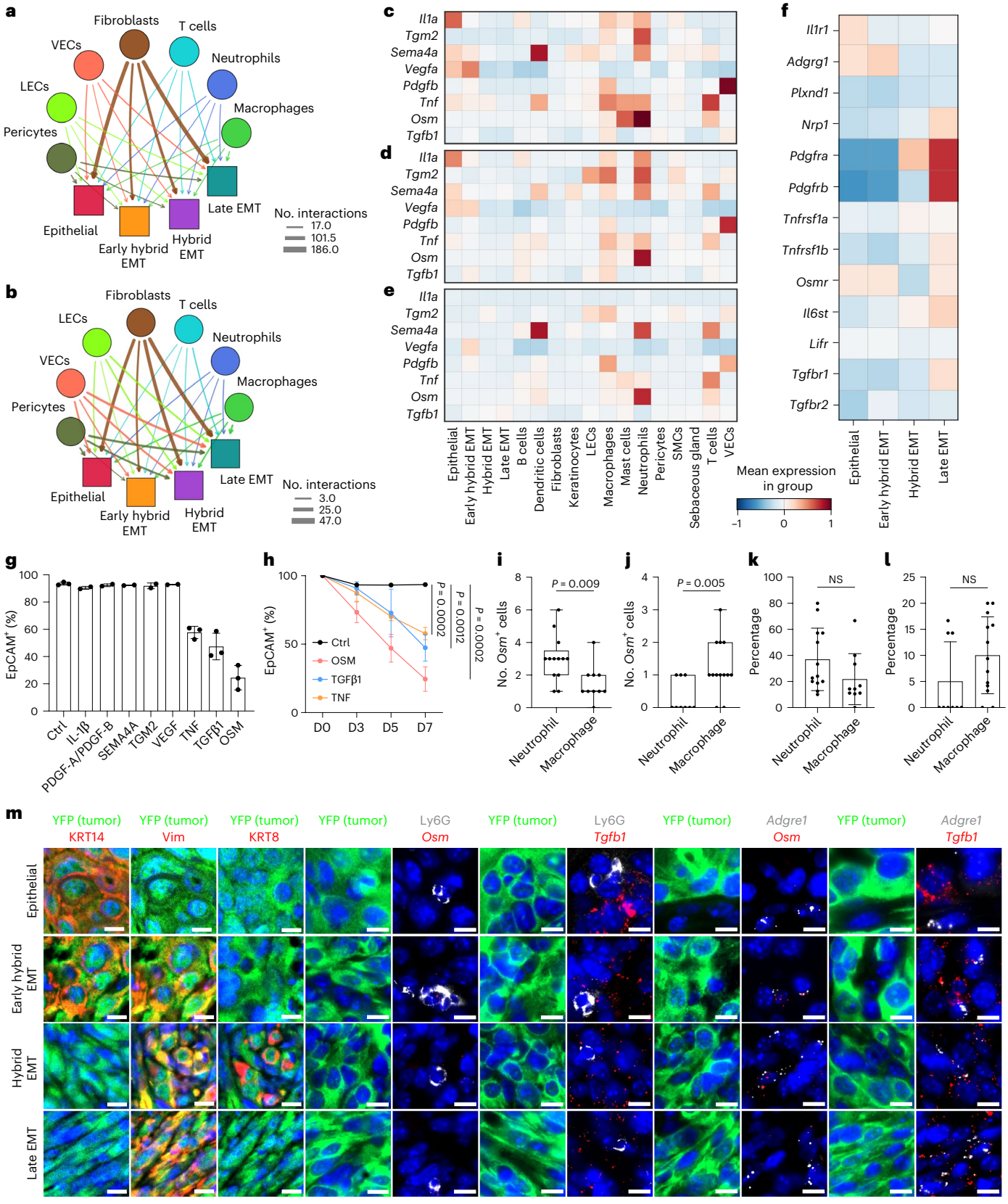

https://doi.org/10.1038/s43018-026-01259-3

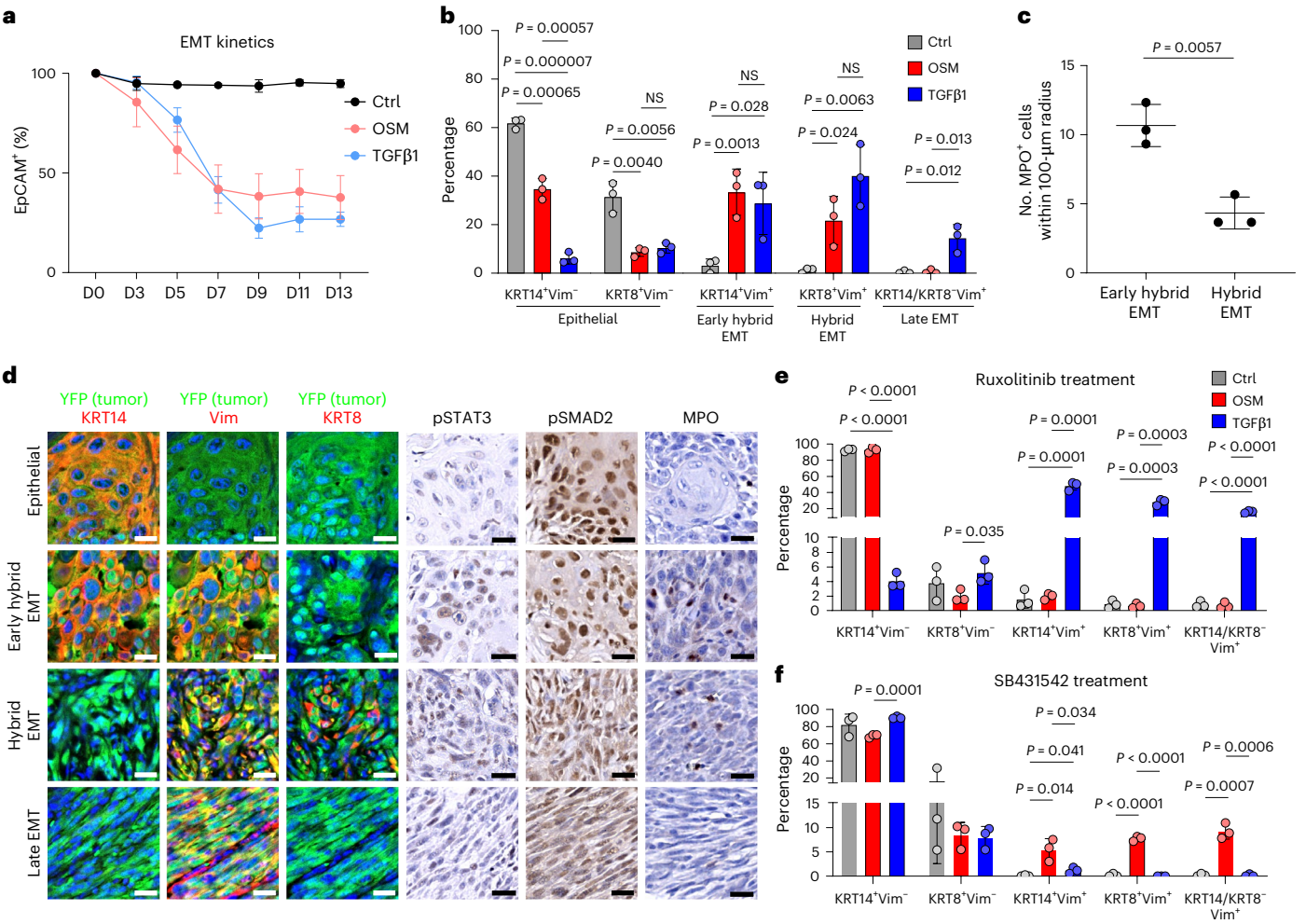

Fig. 6 | OSM and TGFβ1 promote different EMT states. a, Time course analysis of EpCAM percentage in mouse skin SCC-derived cells during treatment with OSM or TGFβ1 (1 ng ml^{-1}) or under control conditions; $n = 3$ independent experiments per condition. Data represent the mean ± s.d. **b**, Cytospin immunostaining quantification of KRT14, KRT8 and vimentin at day 13 under control conditions ($n = 3$ independent experiments, 759 cells analyzed) or with OSM ($n = 3$ independent experiments, 881 cells analyzed) or TGFβ1 treatment ($n = 3$ independent experiments, 606 cells analyzed). Data represent the mean ± s.d., analyzed using multiple *t*-tests. **c**, Quantification of the abundance of neutrophils (MPO$^+$ cells) in a 100-µm radius of pSTAT3^{hi} regions in early hybrid and hybrid EMT states. Data show average counts of three regions of interest from three tumors per state. Data represent the mean ± s.d., analyzed using a two-sided unpaired *t*-test with Welch's correction. **d**, Immunohistochemistry showing pSTAT3, pSMAD2 and MPO staining in mouse skin SCC tumor sections with different EMT states; scale bars, 20 µm. Immunofluorescence was performed in sequential sections and as triple staining for YFP/vimentin/KRT14 and YFP/vimentin/KRT8. Representative images are shown from three tumors per EMT state, with similar results obtained in each tumor. **e**,**f**, Cytospin immunostaining quantification of KRT14, KRT8 and vimentin at day 13 following treatment with ruxolitinib (**e**; 100 nM) or SB431542 (**f**; 100 nM) in control cells or cells treated with OSM or TGFβ1; $n = 3$ independent experiments per condition. For ruxolitinib: control $n = 3$, 1,154 cells analyzed; OSM $n = 3$, 993 cells analyzed; TGFβ1 $n = 3$, 1,137 cells analyzed. For SB431542: control $n = 3$, 1,344 cells analyzed; OSM $n = 3$, 982 cells analyzed; TGFβ1 $n = 3$, 643 cells analyzed. Data represent the mean ±s.d. and were analyzed using multiple *t*-tests.

squamous differentiation genes (*Ivl* and *Krt14*/*Krt16*/*Krt17*/*Krt19*) and strongly induced the expression of *Trp63*, the master regulator of epidermal differentiation[52] (Fig. 7d and Extended Data Fig. 8f). TGFβ1 instead promoted late EMT genes[5,9,53–55] (*Itgb3*, *Acta2*, *Ntn1* and *Grem1*), ECM remodeling genes (*Mmp9*, *Col27a1* and *Col12a1*) and angiogenic/lymphangiogenic genes (*Vegfa*, *Pdgfb* and *Vegfc*; Fig. 7e–g). In addition, OSM upregulated the expression of its own receptor, *Osmr*, whereas TGFβ1 did not upregulate *Tgfbr1*/*Tgfbr2* (Extended Data Fig. 8g). Ruxolitinib reduced OSM-induced *Snai1* and *Trp63* expression, whereas SB431542 strongly repressed TGFβ1-induced *Zeb1* expression (Extended Data Fig. 8h,i).

Gene set enrichment analysis (GSEA) using scRNA-seq-derived EMT state signatures confirmed that OSM preferentially induced the early hybrid EMT signature, with later EMT progression only in EpCAM^{mid}/EpCAM^{neg} cells, while TGFβ1 did not affect EpCAM^{hi} cells but strongly induced a late EMT signature in EpCAM^{mid}/EpCAM^{neg} populations (Extended Data Fig. 8j–l).

Signature scoring using the upregulated genes induced by either OSM or TGFβ1 in our scRNA-seq dataset revealed enrichment of the OSM signature in the early hybrid and late EMT states, increasing from epithelial to mesenchymal tumors, while the TGFβ1 signature was largely restricted to the late EMT state and increased specifically in mesenchymal tumors (Extended Data Fig. 8m,n). The OSM signature correlated positively with neutrophil abundance in mixed tumors, while the TGFβ1 signature correlated with fibroblasts, macrophages and VECs (Extended Data Fig. 8o,p), supporting the notion that neutrophils are the primary source of OSM signaling in early hybrid EMT cells.

Both cytokines reprogrammed cellular metabolism: OSM broadly upregulated glycolysis and xenobiotic detoxification while suppressing steroid biosynthesis and mitochondrial substrate oxidation, whereas TGFβ1 had a narrower, largely overlapping effect with OSM (Extended Data Fig. 8q). These changes were largely independent of EpCAM status, suggesting that the metabolic reprogramming is mediated by the

https://doi.org/10.1038/s43018-026-01259-3

downstream signaling pathways rather than through their promotion of specific EMT states.

OSM induced the expression of neutrophil-recruiting chemokines (*Csf3*, *Cxcl3* and *Cxcl5*), which were downregulated by TGFβ1. Additionally, TGFβ1 induced the expression of macrophage-recruiting factors (*Csf1*, *Ccl2*, *Ccl7* and *Cx3cl1*; Fig. 7h). Conditioned medium from OSM-treated tumor cells enhanced neutrophil migration in transwell migration assays, while conditioned medium from TGFβ1-treated cells enhanced macrophage chemotaxis (Fig. 7i,j). Administration of antibodies blocking OSM to mice bearing transplanted primary SCCs

Fig. 7 | OSM and TGFβ1 regulate distinct EMT transcriptional programs and create distinct niches to maintain hybrid and late EMT states. a, PCA plot showing the distribution of the bulk RNA-seq dataset from different EpCAM populations collected on day 13 from a mouse skin SCC-derived cell line under control conditions or following OSM or TGFβ1 treatment; $n = 3$ independent experiments per condition. **b**–**h**, Bar charts showing the mRNA expression of epithelial and mesenchymal genes (**b**), EMT TFs (**c**), genes associated with squamous differentiation (**d**), late EMT state (**e**), ECM/stiffness (**f**), angiogenesis (**g**) and myeloid cell recruitment (**h**) across EpCAM populations and treatment conditions; $n = 3$ independent experiments per condition. Data represent the DESeq2 $\log_2$ (fold change) ± s.e.; FC, fold change. **i**,**j**, Percentage of migrated neutrophils (**i**) and macrophages (**j**) in transwell assays using conditioned medium collected from day 13 control-, OSM- or TGFβ1-treated cells ($n = 3$ independent experiments per condition). Data represent the mean ± s.d., analyzed using a two-sided unpaired *t*-test with Welch's correction. **k**, Cytospin immunostaining quantification of KRT14, KRT8 and vimentin from transplanted tumors following anti-IgG ($n = 5$ mice, 1,401 cells analyzed), anti-OSM ($n = 4$ mice, 1,238 cells analyzed) or anti-pan-TGFβ treatment ($n = 3$ mice, 443 cells analyzed). Data represent the mean ± s.d., analyzed using multiple *t*-tests.

reduced the early hybrid EMT state, increased the late EMT state and reduced neutrophil infiltration (Fig. 7k and Extended Data Fig. 9a–d), further showing that OSM promotes neutrophil recruitment and maintains the hybrid EMT states in vivo. By contrast, administration of pan-TGFβ blocking antibodies accelerated tumor growth and inhibited EMT progression, indicating a dominant role of TGFβ in promoting EMT progression (Fig. 7k and Extended Data Fig. 9b).

Together, these results show that OSM and TGFβ1 activate distinct transcription programs to recruit different myeloid populations and establish distinct inflammatory niches that maintain specific EMT states.

OSM-driven EMT niches in human cancer

To investigate whether the OSM-driven niche is also present in human tumors, we analyzed two publicly available Xenium 5K Prime datasets: a human breast cancer dataset and a FOLFIRINOX/nivolumab-treated pancreatic ductal adenocarcinoma (PDAC) dataset selected for elevated EMT[56]. In breast cancer, we identified standard immune and stromal populations alongside five tumor transcriptional states (apart from proliferative state) by marker gene expression and hallmark EMT signature enrichment (Fig. 8a and Extended Data Fig. 10a,b): epithelial, luminal, secretory, stress-hybrid (*FOSL1*$^+$, *SMAD3*$^+$, *SNAI1*$^+$) and invasive-hybrid (*ERBB2*$^+$, *VEGFA*$^+$, *L1CAM*$^+$), the latter two showing the highest EMT enrichment. TNF/NF-κB and TGFβ signaling scores (proxies for OSM- and TGFβ1-induced programs) were both highest in the stress-hybrid cluster (Fig. 8b). Consistent with mouse SCC, OSM expression was restricted to neutrophils and macrophages (Extended Data Fig. 10c), both significantly enriched in the stress-hybrid niche (Fig. 8g), and spatial ligand–receptor analysis identified significant OSM–IL-6ST communication in this cluster (Fig. 8c and Extended Data Fig. 10g,h), supporting an OSM-driven EMT niche in human breast cancer.

The PDAC dataset showed similar TME composition, with a lower overall tumor cell abundance (Extended Data Fig. 10d). Tumor cell subclustering identified six transcriptional states and a proliferating fraction, of which only the EMT state (*MMP14*$^+$, *SNAI2*$^+$, *COL17A1*$^+$) showed significant hallmark EMT enrichment (Fig. 8d). Both TNF/NF-κB and TGFβ signatures were strongly enriched in the EMT state, with additional TGFβ elevation in the squamous cluster (Fig. 8e). OSM expression was again restricted to macrophages and neutrophils, both enriched in the EMT niche (Fig. 8h and Extended Data Fig. 10f), with spatial ligand–receptor analysis confirming OSM–IL-6ST communication associated with the EMT cluster (Fig. 8f and Extended Data Fig. 10i,j), supporting the existence of the OSM-driven EMT niche in human PDAC.

We further validated the OSM-associated niche in patient-derived xenografts (PDXs) presenting different degrees of EMT. In a keratin$^-$, late EMT lung spindle cell carcinoma PDX, macrophages dominated the myeloid niche with few neutrophils (Fig. 8i). Conversely, a hybrid EMT (keratin$^+$vimentin$^+$) lung adenocarcinoma PDX showed increased neutrophil abundance and fewer macrophages. *Osm*-expressing neutrophils were enriched in the hybrid EMT PDX and were associated with pSTAT3$^+$ tumor cells (Fig. 8j–l). By contrast, *Tgfb1* was mainly macrophage derived, and no difference in pSMAD2 expression was observed between mesenchymal and hybrid EMT PDXs (Fig. 8j,m,n), supporting that distinct EMT states are associated with different myeloid populations in human PDX models.

Finally, in a cohort of human urothelial cancers scored for hybrid EMT (coexpression of keratin and vimentin)[57], tumors with higher hybrid EMT scores showed more neutrophil infiltration (Fig. 8o–q), higher pSTAT3 expression (Fig. 8r) and niches enriched in *OSM*-expressing neutrophils and macrophages (Fig. 8s,t), demonstrating that the *OSM*-expressing myeloid niche is found in proximity to hybrid EMT tumor cells.

Together, these data demonstrate that at least in a subset of human cancers, neutrophil- and macrophage-derived OSM signaling is preferentially associated with hybrid EMT states.

Discussion

In this study, we unravel the tumor ecosystem associated with distinct EMT states and identified specific myeloid-derived signals that establish distinct stromal niches regulating these states.

Early hybrid EMT cells reside in a neutrophil-enriched niche, whereas later EMT stages show neutrophil absence alongside more abundant macrophages and endothelial cells. Integrating scRNA-seq data with spatial transcriptomics, we uncover that EMT states are not only defined by intrinsic transcriptional programs but also actively maintained by spatially organized, myeloid-driven niches. We identify OSM and TGFβ1 as the key extrinsic orchestrators of the hybrid and late EMT niches, respectively, operating through self-reinforcing feed-forward loops that stabilize specific EMT states.

OSM acts in a paracrine manner to simultaneously activate two apparently opposing transcriptional programs. OSM upregulates the EMT inducers SNAI1 and ZEB1 (ref. 1) and ΔNP63, the master regulator of squamous epithelial identity[52], as well as KLF5, a key regulator of the

Fig. 8 | OSM-driven stromal niches are present in human tumors. a, Heat map displaying the mean expression of marker genes across tumor cell states in the breast tumor. The color scale represents scaled mean expression within each cell state. **b**, Hallmark pathway enrichment scores for EMT, TNF signaling via NF-κB (TNF) and TGFβ signaling across tumor states of the breast tumor. **c**, Heat map of ligand–receptor interaction scores for OSM and its receptors across breast tumor states. **d**–**f**, As in **a**–**c**, respectively, but for the PDAC tumor. **g**,**h**, Neighborhood enrichment analysis showing spatial colocalization between stromal and immune cell types and tumor states in breast (**g**) and PDAC (**h**) tumors; *z*-scores indicate enriched proximity (red, positive) or spatial exclusion (blue, negative); $n = 1$ tumor for **a**–**h**. **i**,**j**, Immunofluorescence of neutrophils and macrophages (**i**) and immunohistochemistry of pSTAT3 and pSMAD2 (**j**) in PDXs of lung spindle cell carcinoma and lung adenocarcinoma; scale bars, 20 µm; CK, cytokeratin. **k**–**n**, RNAscope analysis of *Osm*-expressing neutrophils (**k**) and macrophages (**l**) and *Tgfb1*-expressing neutrophils (**m**) and macrophages (**n**) in PDXs of lung spindle cell carcinoma and lung adenocarcinoma; scale bars, 5 µm. **o**–**r**, Immunofluorescence of pan-cytokeratin and vimentin (**o**) and immunohistochemistry of CD68 (**p**), CD15 (**q**) and pSTAT3 (**r**) in samples from individuals with urothelial cancer stratified by low and high EMT scores; scale bars, 100 µm. **s**,**t**, RNAscope analysis of *OSM*-expressing neutrophils (**s**) and macrophages (**t**) in samples from individuals with urothelial cancer stratified by low and high EMT scores; scale bars, 20 µm. Representative images are shown from $n = 3$ PDX tumors per tumor type (**i**–**n**) and $n = 3$ samples from individuals with urothelial cancer per tumor type (**o**–**t**), with similar results obtained in each experiment; IFN, interferon.

https://doi.org/10.1038/s43018-026-01259-3

epithelial/early hybrid EMT state[10]. The coactivation of these opposing transcriptional programs provides a mechanistic explanation for the hybrid nature of the OSM-induced state, in which cells retain partial epithelial identity while acquiring mesenchymal features.

The OSM-associated niche presents a self-reinforcing architecture: neutrophil-derived OSM induces tumor cells to upregulate OSMR expression and produce neutrophil-attracting chemokines (*Csf3*, *Cxcl3* and *Cxcl5*)[36], recruiting further neutrophils and perpetuating OSM signaling. Although OSM has been shown to reprogram CAFs to recruit myeloid cells in pancreatic and breast cancer[31,58], its neutrophil-specific niche-organizing function in controlling a defined EMT state has not been previously reported. Our data support a bidirectional model, in which initial partial EMT facilitates early neutrophil recruitment, after which neutrophil-derived OSM consolidates and amplifies this

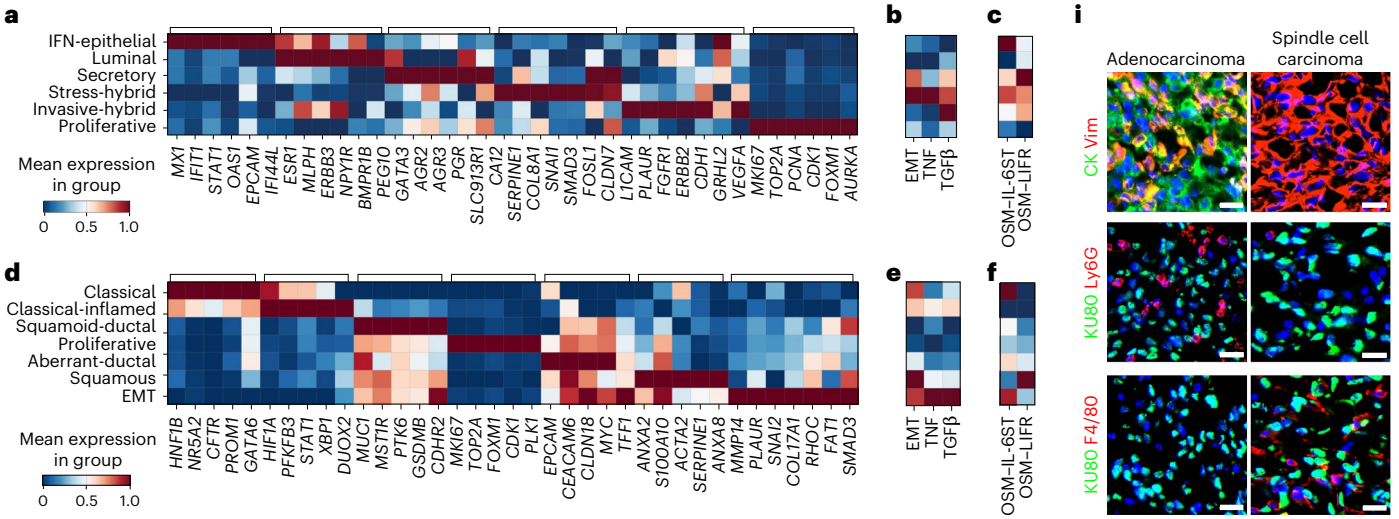

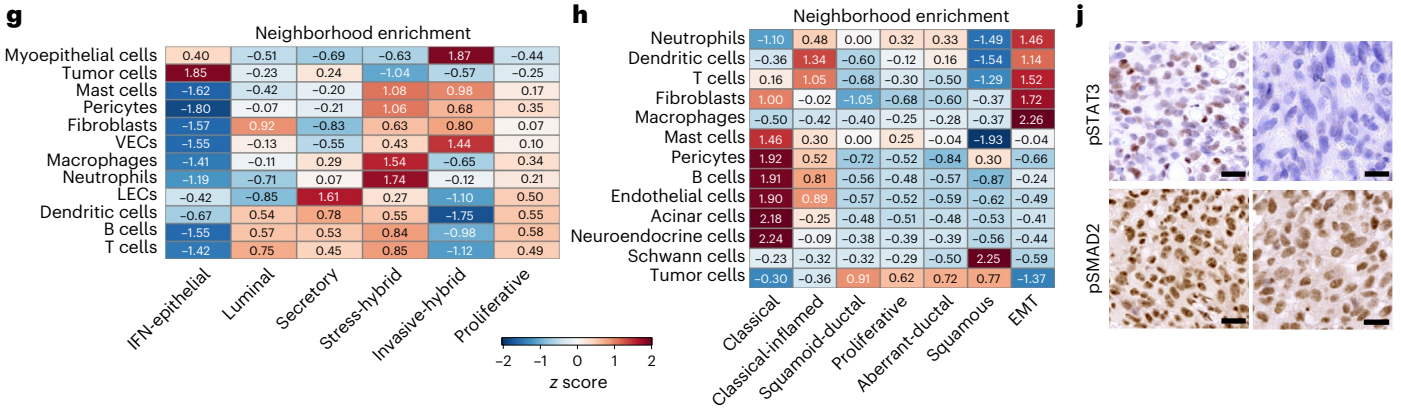

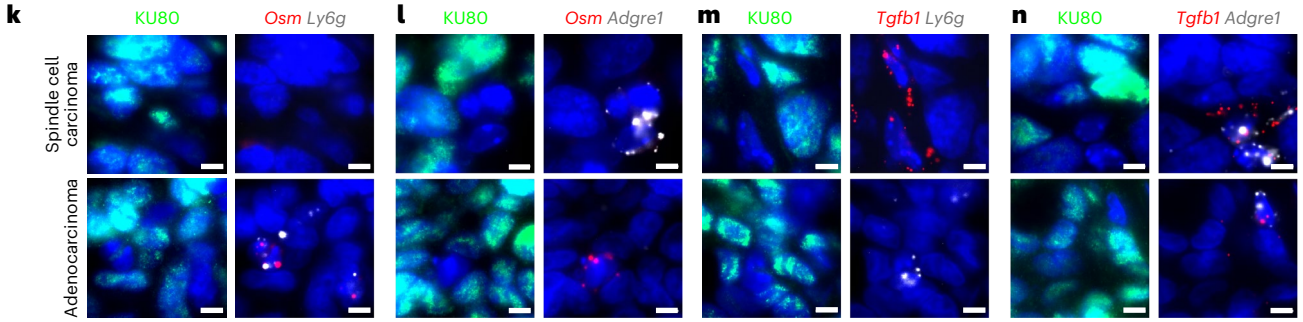

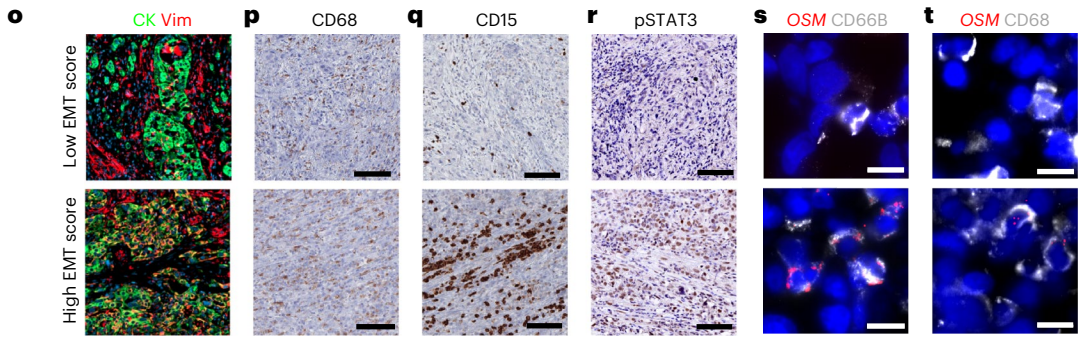

hybrid state. Both neutrophil depletion and OSM blockade reduced the hybrid EMT population and shifted tumors toward late EMT in vivo, demonstrating that neutrophils actively maintain this hybrid state and suggesting that, unlike in vitro settings, OSM is not required for EMT initiation in vivo. This discrepancy could be explained by the dominant role of TGFβ and redundancy of EMT-inducing signals in vivo. Neutrophil depletion also reduced metastatic burden, consistent with the established prometastatic properties of hybrid EMT states[5–7,37], linking the neutrophil-associated niche to metastatic dissemination.

A recent study linked neutrophil-driven vascular occlusion and necrosis to prometastatic niches in breast cancer[59]. However, we did not observe extensive necrosis in our mouse tumor model, and, despite high neutrophil infiltration, the early hybrid EMT niches are not highly hypoxic (Extended Data Fig. 4l), suggesting that neutrophil recruitment in our model is not mediated by vascular occlusion.

The initiating event for inducing this niche remains unresolved. One possibility is that stochastic genetic or epigenetic alterations first induce a partial EMT program that promotes neutrophil recruitment, after which neutrophil-derived OSM reinforces and stabilizes the hybrid EMT state. Alternatively, inflammatory or myeloid-derived cues from infiltrating myeloid cells may precede and initiate EMT state transitions through OSM or TGFβ1 signaling. These scenarios are not mutually exclusive and may coexist. It is also possible that low-level activation of both OSM and TGFβ signaling occurs during establishment of the early hybrid EMT state, with their relative contributions evolving as tumors progress toward later EMT states. Lineage-tracing approaches together with dynamic OSM and TGFβ1 pathway reporters will be required to resolve the temporal sequence leading to establishment of these distinct inflammatory niches.

Our study confirmed the established role of TGFβ1 as a key EMT mediator and, additionally, uncovered its function in establishing the late EMT macrophage-enriched niche, which is sustained through a feed-forward loop by late EMT cells upregulating macrophage-recruiting chemokines. Functional perturbation experiments revealed distinct roles for each pathway. OSM blockade reduces the hybrid state but unexpectedly promotes progression toward late EMT. TGFβ inhibition restricts tumors to a predominantly epithelial state at the cost of accelerated tumor growth, revealing a potential therapeutic trade-off between EMT suppression and limiting primary tumor burden.

Spatial transcriptomics of human breast cancer and PDAC revealed OSM expression in neutrophils and macrophages analogous to mouse SCC, with significant OSM–IL-6ST signaling to hybrid EMT tumor cells in both. In PDXs, hybrid EMT cells colocalized with *Osm*-expressing neutrophil niches and high pSTAT3, while late EMT tumors were enriched for macrophages. Similarly, human urothelial tumors with high hybrid EMT scores associated with increased myeloid infiltration and pSTAT3 activity, showing that the neutrophil-associated hybrid EMT niche is found in a subset of human cancers, including breast cancer, PDAC and urothelial carcinoma; whether it extends to human cutaneous SCC remains to be assessed.

Despite these complexities, the OSM–hybrid EMT axis has clear translational relevance. Hybrid EMT states are linked to chemotherapy resistance across different cancers[5–7,37], and OSM–OSMR signaling is associated with therapy resistance in lung and breast cancer[27,60]. By simultaneously activating EMT TFs while preserving epithelial identity, OSM establishes an intermediate state whose phenotypic plasticity may enhance adaptability under therapeutic stress. Future studies in clinically relevant models will be required to determine whether and how modulation of these pathways can be therapeutically exploited.

In summary, our study demonstrates that distinct EMT states are actively organized and maintained by spatially defined myeloid-derived cytokine niches through feed-forward loops in which myeloid-derived signals orchestrate both specific EMT transcriptional programs and the spatial architecture of the TME.

Methods

Compliance with ethical regulations

Mice were housed in a certified animal facility according to European guidelines and the European Convention for the Protection of Vertebrate Animals used for Experimental and other Scientific Purposes (ETS 123). All experiments were approved by the Commission d'Etique et du Bien-être Animal, Faculty of Medicine, Université Libre de Bruxelles, under licenses 828N, 915N and 916N. Written informed consent for sample collection, research and publication of deidentified data was obtained from all individuals whose samples were used for PDX generation. Human urothelial samples used in this study consisted of residual biological material maintained in our tissue bank. Residual material corresponds to the excess tissue that was not required for the individual's diagnosis. This tissue is stored as paraffin blocks at a controlled temperature (+20 °C) for a 20-year retention period in accordance with Belgian legislation. All samples were used under an opt-out consent model, whereby participants are presumed to agree to the research use of their residual biological material unless they explicitly object; no opt-out had been registered for any participant included in this study.

Mice were monitored daily and killed at predefined endpoints, including a tumor diameter of 1 cm, ulceration irrespective of tumor size, >20% body weight loss or signs of distress. No tumor exceeded the permitted size or burden. Mice were housed at 20–24 °C with 55 ± 10% relative humidity on a 12-h light/12-h dark cycle, with food, water and two types of nesting material available.

Mouse strains and genetically induced skin SCC

Rosa26-YFP mice[61], *Lgr5*^{creER} mice[62], *Kras*$^{LSL\text{-}G12D}$ mice[63] and *Trp53*$^{fl/fl}$ mice[64] were imported from the National Cancer Institute mouse repository and Jackson Laboratories. NOD/*scid* and NOD/*scid*/*Il2rg*-null mice were purchased from Charles River. Mice of both sexes and mixed genetic backgrounds were used. No randomization or blinding was performed.

The genetically induced skin SCC model was generated by crossing *Rosa26*-YFP[61], *Lgr5*^{creER}[62], *Kras*$^{LSL\text{-}G12D}$[63] and *Trp53*$^{fl/fl}$[64] mice as previously described[65]. At postnatal day 28, LKPR mice received four consecutive daily intraperitoneal injections of tamoxifen (2.5 mg per dose, 25 mg ml^{-1} in sunflower seed oil (Sigma, T5648-1G) containing 10% ethanol) to induce CreERT2-mediated recombination in *Lgr5*-expressing hair follicle cells, activating *Kras*^{G12D}, deleting *Trp53* and inducing YFP expression. Tumor growth was monitored daily using precision calipers, and mice were killed at the predefined endpoint or when distress signs were observed (around 13–16 weeks old).

Cell culture and ligand stimulation

Primary EpCAM^{+} LKPR tumor cells isolated by FACS were cultured in MEM (Capricorn Scientific, SP-2002-500ml) containing 10% FBS (Gibco, 10437-028), 4 µg ml^{-1} hydrocortisone (Sigma, H0888), 1% penicillin/streptomycin (100×; Capricorn Scientific, PS-B), 2 mM L-glutamine and 500 µl of T3 (Sigma, T6397). Cells were washed with DPBS (1×) and detached using trypsin (Capricorn Scientific, TRY-2B10).

For screening of EMT-inducing ligands, cells were treated every 2 days with TGFβ1 (Peprotech, 100-21), OSM (Biotechne, AF662-SP), TNF (Biotechne, 410-MT-010), IL-1β (Biotechne, 401-ML-005), PDGF-AB (10839-AB-010), semaphorin 4A (Biotechne, 11096-S4-050), TGM2 (5418-TG-010) or VEGF (493-MV-005) under the same culture conditions. RAW264.7 macrophages were purchased from ATCC (TIB-71) and cultured in DMEM (A&E Scientific, E0500-160) containing 10% FBS and 1% penicillin/streptomycin.

FACS isolation and analysis

Tumors were digested in collagenase I (Sigma) at 3.5 mg ml^{-1} in HBSS (Gibco) for 1 h at 37 °C on a rocking plate protected from light. EDTA was added to a final concentration of 5 mM. Cell suspensions were washed with PBS containing 10% FBS, filtered through a 70-µm cell strainer

(BD Biosciences) and centrifuged at 300*g* for 10 min at 4 °C. Cells were stained with antibodies to CD45, CD31 and EpCAM (Supplementary Table 2) for 30 min at 4 °C, washed, centrifuged at 600*g* for 5 min at 4 °C and resuspended in Hoechst 33342 trihydrochloride trihydrate (Invitrogen, H3570; 1:4,000), followed by filtration through a 40-µm cell strainer (BD Biosciences). Live singlet cells were identified using forward and side scatter profiles, doublet discrimination and exclusion of dead cells. Tumor cells were identified as YFP^+ and $CD45^-CD31^-$ (Lin^-), and EpCAM expression was assessed within the YFP^+Lin^- population.

FACS analysis and sorting were performed using FACSAria and LSR-Fortessa instruments and FACSDiva software (v.9.1, BD Biosciences). Sorted cells were collected in culture medium containing 50% FBS for cell line establishment, lysis buffer for RNA extraction or PBS containing 0.04% filtered BSA for single-cell sequencing. Established cell lines were stained with anti-EpCAM and Hoechst 33342 trihydrochloride trihydrate, and live single YFP^+EpCAM^{hi}, YFP^+EpCAM^{mid} or YFP^+EpCAM^{neg} populations were isolated (Supplementary Fig. 1a and Extended Data Fig. 7a).

Dual single guide RNA cloning and knockout validation

Dual single guide RNA (sgRNA) constructs were generated using a one-step cloning protocol[10]. Briefly, annealed sgRNAs (Supplementary Table 3) were sequentially cloned into the pLenti_dual-hU6-sgRNA-mU6-sgRNA-EF1a-mCherry-P2A-PuroR backbone using Esp3I and BbsI restriction sites. For lentivirus production, HEK 293T cells (ATCC, CRL-3216) were transfected with psPAX2 and pMD2.G packaging plasmids using Lipofectamine 2000. Viral supernatants were collected 48–72 h after transfection, concentrated with PEG-8000 and used for transduction in the presence of polybrene (10 µg ml^{-1}). Genomic DNA was extracted using the QIAamp DNA Mini Kit (Qiagen, 51306) with 200 µl of PBS and 20 µl of proteinase K for digestion. Gene-specific PCR primers (Supplementary Table 3) were used to detect genomic deletions, and PCR products were analyzed on 2% agarose gels.

Real-time quantitative PCR with reverse transcription

RNA from tumor cells isolated by FACS was extracted using the RNeasy Micro Kit (Qiagen), with on-column DNase treatment. cDNA was synthesized using the RevertAid First Strand cDNA Synthesis Kit (Thermo Fisher). Real-time quantitative PCR with reverse transcription was performed using SYBR Green Supermix (Applied Bioscience) on a LightCycler 96 system (Roche). Relative gene expression was normalized to *Tbp* with corresponding qPCR primers (Supplementary Table 3).

Inducible overexpression of *Osm* and *Tgfb1* in macrophages

Mouse *Osm* or *Tgfb1* cDNA was cloned into the pLVX-TetOne-Puro vector, with the empty vector used as a control. Lentivirus was produced and used to transduce RAW264.7 macrophages as described above, followed by puromycin selection. For co-transplantation, 1,000 tumor cells were subcutaneously injected alone or mixed with 100 macrophages carrying *Osm*, *Tgfb1* or the empty vector into recipient mice as described above. Doxycycline was administered in drinking water (2 g l^{-1} doxycycline and sucrose) following transplantation until the animals were killed. All experimental groups received doxycycline.

Tumor transplantation and metastasis assays

YFP^+EpCAM^+ cells isolated by FACS from primary LKPR tumors were collected in a 1:1 mixture of culture medium and FBS and maintained at 4 °C. Cells were resuspended in a 1:1 mixture of FBS and Matrigel (E1270, 970 mg ml^{-1}; Sigma) and subcutaneously injected into both male and female NOD/*scid*/*Il2rg*-null mice aged 7–8 weeks, at 1,000 cells per injection site. For PDX transplantation, tumors were cut into 3 × 3 × 3 mm pieces and inserted into the fat pad of both male and female NOD/*scid* mice aged 7–8 weeks in 100 µl of Matrigel solution. For co-transplantation experiments, 1,000 tumor cells were mixed with 100 *Osm*-overexpressing, *Tgfb1*-overexpressing or empty vector control macrophages before injection. Tumor growth was monitored weekly by palpation and caliper measurement. Mice were killed when tumors reached 1 cm in diameter or when signs of distress were observed.

For metastasis assays, lungs were collected 6 weeks after resection of subcutaneous tumors and processed for cryosectioning. Metastatic lesions were identified by YFP fluorescence and quantified in three cryosections per lung. Metastatic burden was measured as the number of metastatic lesions per lung and the relative metastatic area using ZEN Microscopy Software.

In vivo antibody treatment

Antibody treatments were initiated immediately after subcutaneous transplantation and continued until the mice were killed for metastasis analysis. For macrophage depletion, mice received intraperitoneal injections of 300 µg of anti-CSF1R (clone AFS98, Bio X Cell, BE0213) and 200 µg of anti-CCL2 (clone 2H5, Bio X Cell, BE0185) every 4 days. For neutrophil depletion, mice received 50 µg of anti-Ly6G (clone 1A8, Bio X Cell, BP0075-1) daily, together with 50 µg of anti-rat immunoglobulin κ-chain (clone MAR 18.5, Bio X Cell, BE0122) every other day. Control mice received control antibody (clone 2A3, Bio X Cell, BE0089) on the same schedule. For TGFβ blockade, mice received 500 µg of anti-pan-TGFβ (clone 1D11.16.8, Bio X Cell, BE0057) every 4 days during the first week, followed by 250 µg every 2 days. For OSM blockade, mice received 500 µg of anti-OSM (clone 24A8, Genentech) twice weekly. Corresponding control mice received control antibody (clone MOPC-21, Bio X Cell, BE0083).

Cytospin, immunofluorescence and histology

Cytospin preparations were generated using CellspinI (Tharmac), with 20,000 cells per cytospin. Tumor tissues were fixed in 4% paraformaldehyde (PFA) for 4 h at room temperature, washed in PBS, incubated overnight in 30% sucrose at 4 °C, embedded in OCT (Tissue-Tek) and cryosectioned at 6 µm. Cytospin preparations were fixed in 4% PFA for 10 min at room temperature.

For immunofluorescence, samples were blocked for 1 h at room temperature in PBS containing 5% horse serum, 1% BSA and 0.2% Triton X-100. Primary antibodies (Supplementary Table 2) were incubated overnight at 4 °C, followed by three PBS washes and incubation with secondary antibodies for 1 h at room temperature. Nuclei were counterstained with Hoechst 33342 trihydrochloride trihydrate (1:4,000), and slides were mounted using SafeMount (Labonord). Images were acquired using a Zeiss Axio Imager M2 fluorescence microscope and Axiovision software (4.8). For cell density analysis, marker-positive cells were counted within standardized 250 × 250 µm (0.0625 mm^2) regions of interest, and density was calculated as cells per mm^2 using identical region of interest dimensions and counting criteria across groups.

For human tissue analysis, archival formalin-fixed paraffin-embedded (FFPE) samples meeting ISO15189 standards were selected from the institutional biobank by a pathologist. Four-micron sections were subjected to multiplexed immunofluorescence using a Ventana Discovery Ultra (Ventana Medical Systems). Mouse tumor tissues were fixed overnight in 4% PFA at 4 °C, embedded in paraffin and subjected to citrate buffer (pH 6.0) antigen retrieval. Sections were incubated overnight at 4 °C with primary antibodies (Supplementary Table 2), washed and incubated for 30 min at room temperature with the corresponding biotinylated secondary antibodies. Horseradish peroxidase activity was detected using a standard ABC kit and ImmPACT DAB substrate (Vector Laboratories). Sections were counterstained with Mayer's hematoxylin (Labonord), dehydrated and imaged using a ZEISS Axioscan 7 digital slide scanner.

Second harmonic generation

One hundred-micron-thick sections from OCT-embedded tissue were blocked in PBS containing 1% BSA, 5% horse serum and 1% Triton X-100 for 3 h at room temperature. Sections were incubated overnight at

room temperature with antibodies to GFP and ACTA2, washed with PBS containing 0.2% Tween-20 and incubated for 1 h at room temperature with secondary antibodies and Hoechst 33342 (1:4,000). Sections were subsequently washed and mounted in Dako mounting medium. Images were acquired using an LSM 880 confocal microscope (Zeiss) mounted on an AxioObserver 7 NLO inverted microscope (Zeiss). Multiphoton excitation was provided by a tunable InSight X3 laser (Spectra-Physics) at 880 nm. Serial optical sections were collected using a Plan-Apochromat ×40/0.95-NA dry objective (Zeiss) with a 2.0-µm *z* step. Images were stitched and analyzed using ZEN 3.10 software (Zeiss), and maximum intensity projections were generated.

Immunoblot analysis

Cells were washed with ice-cold PBS and lysed in SDS-containing lysis buffer. Lysates were sonicated using a Bioruptor Plus sonicator (Diagenode, UCD-300) and centrifuged at 10,000*g* for 15 min at 4 °C. Protein concentrations were determined using the Pierce 660-nm Protein Assay Kit (Thermo Fisher Scientific, 22662) with Ionic Detergent Compatibility Reagent (Thermo Fisher Scientific, 22663). Equal amounts of protein (10–30 µg) were separated on 4–12% SDS–PAGE gels (Thermo Fisher Scientific) and transferred to nitrocellulose membranes. Membranes were blocked with 5% non-fat dry milk and 0.05% BSA for 1 h at room temperature and incubated overnight at 4 °C with primary antibodies (Supplementary Table 2). Membranes were washed with PBS containing 0.05% Tween-20 and incubated for 1 h at room temperature with horseradish peroxidase-conjugated anti-rabbit IgG secondary antibody (NA9340V, Sigma-Aldrich; 1:5,000). Signals were detected using enhanced chemiluminescence reagents (Western Dura or ECL Chemiluminescence System, Pierce) and imaged using an iBright FL1500 imaging system (Invitrogen).

RNAscope

RNAScope was performed according to the manufacturer's instructions (Advanced Cell Diagnostics) on paraffin-embedded mouse skin SCC and FFPE human urothelial tumor sections with the following probes: Mm-Osm (427071-C2), Mm-Tgfb1 (407751-C3), Mm-Adgre1 (460651-C2, 460651-C3), Mm-Ly6g (455701-C2, 455701-C3) and Hs-Osm (456381-C2).

Conditioned medium collection

Primary EpCAM$^+$ LKPR cell lines isolated by FACS were cultured in normal medium or treated with TGFβ1 or OSM (1 ng ml^{-1} every other day) for 13 days. Cells were then collected and reseeded at 50,000 cells per ml in normal medium. After 48 h, conditioned medium was collected and centrifuged at 300*g* for 3 min to remove floating cells and used directly or snap-frozen at −80 °C.

Bone marrow-derived neutrophil isolation

Bone marrow-derived neutrophils were isolated from the femurs and tibiae of wild-type CD-1 mice of both sexes aged 7–8 weeks. The bone marrow was flushed with PBS containing 2% FBS through a 70-µm cell strainer and centrifuged at 300*g* for 10 min at 4 °C. Cells were stained with antibodies to CD45, CD11b and Ly6G, followed by Hoechst 33342 trihydrochloride trihydrate (1:4,000), and filtered through a 40-µm cell strainer. Living single CD45$^+$CD11b$^+$Ly6G$^+$ cells were sorted by FACS (Supplementary Fig. 1b), collected in FBS and immediately seeded into transwell chambers.

Transwell assay

One hundred thousand bone marrow-derived neutrophils or 50,000 RAW264.7 macrophages were seeded in the top chamber of a 24-well transwell plate in 100 µl of culture medium. The bottom chamber contained 600 µl of conditioned medium from cultured tumor cells. Neutrophils were collected after 2 h, and macrophages were collected after 48 h. Migrated cells were recovered from the bottom membrane and holding plate, centrifuged at 300*g* for 3 min and counted using a hemocytometer.

Statistics and reproducibility

Statistical analyses were based on biological replicates, with sample sizes indicated in the text, figures or figure legends. Two-sided unpaired *t*-tests with Welch's correction were used for two-group comparisons, whereas multiple *t*-tests were used for comparisons involving more than two groups. Analyses were performed using GraphPad Prism v9.00. Bar graphs and dot plots show mean ± s.d. No data were excluded. Experiments were not randomized, and the investigators were not blinded during allocation, data collection or outcome assessment. Sample sizes were not determined using formal statistical power calculations but were comparable to those reported in previous publications[9,10]. Data distributions were assumed to be normal but were not formally tested.

ScRNA-seq library preparation and analysis

Following isolation by FACS, primary LKPR cells were sorted into 50% YFP$^+$Lin$^-$, 25% YFP$^-$Lin$^-$ and 25% YFP$^-$Lin$^+$ populations. Cells were collected in PBS containing 0.04% filtered BSA, pelleted at 250*g* for 5 min at 4 °C and resuspended in 50 µl of the same buffer. Samples were loaded onto Chromium Single Cell 3′ microfluidic chips (10x Genomics). Libraries were prepared using the Chromium Single Cell 3′ Library Kit and V2 chemistry (10x Genomics), assessed by low-coverage sequencing on an Illumina NextSeq 550 platform and subsequently sequenced at full-depth on an Illumina NovaSeq.

Ten scRNA-seq samples from primary LKPR tumors were integrated using Scanpy v1.10.2 (ref. 66). Cells were retained when they expressed >700 genes and contained <20% mitochondrial and <30% ribosomal unique molecular identifier counts. Ambient RNA was removed with SoupX v1.6.2 (ref. 67), and doublets were detected using scDblFinder v3.20 (ref. 68). Counts were log normalized, highly variable genes were selected using Scanpy's 'Seurat' flavor, and a PCA was performed. Significant PCs were determined by bootstrapping, and clustering stability was assessed across Leiden resolutions from 0.1 to 1.0 using the cluster R package v0.5.1 (ref. 69). Marker genes were identified using the Wilcoxon rank-sum test, retaining genes expressed in ≥25% of cells with an average log (fold change) of ≥0.25. Cell-type annotation combined Scanpy's module scoring with PanglaoDB marker genes[70] (version 27/03/2020).

Dataset integration was performed using scVI (v1.1.4, n_hidden = 128, n_latent = 50, n_layers = 2, dispersion = 'gene-batch') followed by scANVI[71] to correct batch effects and account for total counts and mitochondrial and ribosomal gene percentages. UMAP and Leiden clustering were performed using the scANVI latent space. Tumor cells were identified based on YFP enrichment, *Kras*^{G12D} and *Trp53* mutations and copy number alterations inferred through inferCNV v1.22.0 (ref. 32).

Subclustering of tumor and TME cells

Tumor cells were subclustered after scaling and regression for cell cycle effects, total counts and mitochondrial and ribosomal percentages. Batch correction was performed using Harmony v1.2.1 (ref. 72), and Leiden clustering used the lowest stable resolution identified with clustree (0.5). EMT states were annotated using *Epcam*, *Krt14*, *Krt8* and *Vim* expression. Bulk RNA-seq-derived *Osm* and *Tgfb1* signatures were computed using Scanpy's score_genes module.

CAFs, macrophages, neutrophils and T cells were independently subclustered using the same general workflow, with Harmony batch correction and cell-type-specific stable clustering resolutions. Cluster annotations were based on marker genes and, for macrophages, signatures from Caronni et al.[35]. Differential was assessed using scCODA in the pertpy v1.0.4 Python package, with an FDR threshold of 0.1. Analyses were performed separately for Lin$^+$ (B cells, dendritic cells, Q19

LECs, macrophages, mast cells, neutrophils, T cells and VECs) and Lin$^-$ populations (adipocytes, fibroblasts, melanocytes, pericytes and Schwann cells).

Cell–cell communication analysis

Ligand–receptor interactions were analyzed using CellPhoneDB[38] and CellChat[39] through the Liana+ v1.6.0 framework[73]. Mouse gene identifiers were converted to human orthologs for compatibility with the CellPhoneDB V5 database. Collagen family members were excluded. Analyses were performed separately for each tumor, and significant interactions were aggregated across samples. Wilcoxon rank-sum tests using a one-versus-all comparison identified ligands associated with EMT states and macrophage or neutrophil recruitment. *P* values were adjusted using the Benjamini–Hochberg method, with an FDR of <0.01 considered significant. Candidate interactions were further filtered based on EMT relevance and published biological support.

Metabolic analysis

Metabolic activity was inferred using scMetabolism (v0.2.1) and scCellFie v0.6.0, excluding adipocytes, B cells and Schwann cells. ScMetabolism was used to score 79 KEGG pathways, followed by sample-level pseudobulk Wilcoxon testing. Pathways were considered significantly differentially active if FDR < 0.05 and | rank-biserial correction | > 0.5. ScCellFie was used to score metabolic tasks with gene expression smoothing and default database thresholds. Metabolic task markers were identified using logistic regression and aggregated using the trimean.

Xenium spatial transcriptomics

FFPE tissue sections were processed according to 10x Genomics guidelines (CG000580, CG000582, CG000584) using Xenium Sample Prep Reagents (PN-1000460) and the Prime 5K probe set. Five tumors (one epithelial, two hybrid and two mesenchymal) were selected for spatial transcriptomic analysis. After hybridization, tissues were quenched, counterstained with DAPI and imaged on the Xenium instrument.

To reduce transcript cross-contamination between adjacent cells, count matrices were generated using only transcripts overlapping nucleus masks rather than the default geometric cell boundary estimates. This approach reduced intercellular contamination but resulted in approximately 50% transcript loss. Cells with <20 mRNA counts or <15 detected genes, as well as the top 2% of cells by total counts, were excluded. Negative-control probes and genes expressed in <100 cells were removed. Data were log normalized, the top 2,000 variable genes were selected, and PCA, nearest-neighbor graph construction, UMAP and Leiden clustering were performed using Scanpy.

Cell type and refined cell state annotation

Major cellular compartments were annotated using marker genes and PanglaoDB gene signature modules, including CAFs, macrophages, neutrophils, dendritic cells, T cells, B cells, pericytes, VECs, LECs, mast cells, smooth muscle cells and sebaceous gland cells. Tumor cells were identified by integrating Xenium expression profiles with immunofluorescence staining and PanglaoDB 'Fibroblasts' and 'Epithelial Cell' modules. Refined cell states were determined by independent re-embedding and subclustering based on published markers, scRNA-seq-derived markers and unbiased differential expression.

For refined analyses, negative-control probes and genes expressed in <1% of cells within each compartment were excluded. The top 2,000 variable genes were used for tumor cells, macrophages and fibroblasts and 1,000 for T cells and neutrophils. PCA, cosine-based nearest-neighbor graphs, UMAPs and Leiden clustering were performed, with stable resolutions determined using clustree. Tumor EMT states were assigned using canonical EMT markers and epithelial markers (*Ovol1*, *Epcam*, *Cdh1*, *Klf5*, *Pitx1* and *Trp63*) and mesenchymal markers (*Cdh2*, *Zeb1*, *Nfatc1*, *Twist1*, *Vcam1*, *Snai1*, *Prrx1*, *Col1a1*, *Pdgfra*, *Col1a2*, *Pdgfrb* and *Postn*).

Spatial neighborhood and ligand–receptor analysis

Spatial neighborhood enrichment was calculated using Squidpy v1.7 (ref. 74) with a 60-µm radius, excluding sebaceous gland, keratinocytes and smooth muscle cells. Neighborhood composition was calculated as the proportion of neighboring cells belonging to each cell-type category, and enrichment was assessed hierarchically at major cell-type and refined subtype levels across EMT states. Each tissue section was divided into 500 spatial blocks, followed by 1,000 block-bootstrap iterations. Statistical significance was assessed using 500 block-level permutations, with EMT state labels shuffled within each block. *P* values were adjusted using the Benjamini–Hochberg procedure.

Spatially informed ligand–receptor interactions were analyzed with LARIS v1 (ref. 75) with the CellPhoneDB V5 database, excluding collagen family members. Analyses used 10 repeats and 10,000 permutations, with spatial weighting, expression filtering and nearest-neighbor permutation parameters. *P* values were adjusted using the Benjamini–Hochberg method, with an FDR of <0.1 considered significant.

Human Xenium spatial transcriptomic datasets

Human Xenium datasets were processed using the same general workflow as the mouse datasets, except that a Leiden clustering resolution of 0.5 was applied for TME and tumor cell clustering. Tumor annotation incorporated established markers, PanglaoDB[70] gene signature modules and the MSigDB[76] hallmark EMT gene signature. The decoupler v1.5 (ref. 77) package with AUCell module was used to score EMT, TNF signaling via NF-κB and TGFβ signaling gene sets. Neighborhood enrichment and spatial ligand–receptor analyses followed the mouse workflow. In the PDAC cohort, sample p15 was selected for detailed analysis based on its highest enrichment for the MSigDB hallmark EMT gene signature across all six profiled participants.

Bulk RNA-seq and analysis

RNA integrity was assessed using the Bioanalyzer 2100 platform (Agilent). Indexed cDNA libraries were generated using the Ovation Solo RNA-seq System (NuGen) and sequenced on a NovaSeq 6000 (Illumina) using HiSeq PE Cluster Kit v4 and TruSeq SBS Kit v3-HS (250 cycles). Approximately 20 million paired-end reads were generated per sample. Read quality was assessed using FastQC, adapters and low-quality regions were removed using Trimmomatic, and processed reads were aligned to the mouse reference genome (Grcm38/mm10) using STAR. Duplicate reads were removed using Picard MarkDuplicates. Genome annotations for Grcm38.87 were retrieved from Ensembl.

Raw counts generated by HTSeq-count were assembled into a gene-by-sample matrix, and Ensembl identifiers were converted to gene symbols. Genes with fewer than ten total counts were excluded. Differential expression was analyzed using DESeq2 through pydeseq2 (v0.5.4), with condition as the design factor, control as the reference and Cook's distance refitting enabled. Variance-stabilizing transformation and PCA were used for quality control. The top 500 positive and negative loading genes from PC1 and PC2 were subjected to MSigDB Hallmark 2020 gene set over-representation analysis using gseapy.enrichr (v1.1.11).

EMT state signatures were derived from the scRNA-seq atlas of ten LKPR tumors by pseudobulk aggregation and one-versus-rest DESeq2 analysis, including tumor of origin as a covariate. Samples contributing fewer than 100 cells to a given state were excluded. Signature genes were defined using an adjusted *P* value of <0.05 and $\log_2$ (fold change) of >0.5, retaining the top 300 genes ranked by Wald statistic. For the early hybrid EMT state, an additional epithelial-versus-early hybrid comparison generated 118 high-confidence signature genes. Signature enrichment was assessed by preranked GSEA, with genes ranked using sign($\log_2$ (fold change)) × $-\log_{10}$ (*P* value) and 1,000 permutations, and by median *z*-score scoring after normalization to counts per million and gene-wise *z* scoring across samples.

Metabolic pathway reprogramming following OSM or TGFβ1 treatment was assessed using preranked GSEA restricted to KEGG metabolic pathways obtained from the KEGG BRITE hierarchy for *Mus musculus* (BRITE ID mmu00001), using the DESeq2 Wald statistic and 1,000 permutations.

Reporting summary

Further information on research design is available in the Nature Portfolio Reporting Summary linked to this article.

Data availability

The scRNA-seq, bulk RNA-seq and spatial transcriptomics data generated in this study have been deposited in the Gene Expression Omnibus (GEO) under accession codes GSE316768 (scRNA-seq), GSE316346 (spatial transcriptomics) and GSE316348 (bulk RNA-seq). These datasets are publicly available. The PDAC spatial transcriptomics dataset (sample p15) is available at GEO under accession code GSE313662. The 10x Genomics Xenium 5K Prime human breast tumor dataset is publicly available from 10x Genomics (https://www.10xgenomics.com/datasets/xenium-prime-ffpe-human-breast-cancer). Source data are provided with this paper.

Code availability

No new code or algorithms were developed for this manuscript. All analyses were performed using previously published, publicly available software packages, as described in the Methods, with parameters specified therein.

References

1. Nieto, M. A., Huang, R. Y.-J., Jackson, R. A. & Thiery, J. P. EMT: 2016. *Cell* **166**, 21–45 (2016).
2. Dong, A. & Blanpain, C. Identification, functional insights and therapeutic targeting of EMT tumour states. *Nat. Rev. Cancer* **26**, 8–26 (2026).
3. Dongre, A. & Weinberg, R. A. New insights into the mechanisms of epithelial–mesenchymal transition and implications for cancer. *Nat. Rev. Mol. Cell Biol.* **20**, 69–84 (2019).
4. Fontana, R., Mestre-Farrera, A. & Yang, J. Update on epithelial–mesenchymal plasticity in cancer progression. *Annu. Rev. Pathol.* **19**, 133–156 (2024).
5. Pastushenko, I. et al. Identification of the tumour transition states occurring during EMT. *Nature* **556**, 463–468 (2018).
6. Simeonov, K. P. et al. Single-cell lineage tracing of metastatic cancer reveals selection of hybrid EMT states. *Cancer Cell* **39**, 1150–1162 (2021).
7. Lüönd, F. et al. Distinct contributions of partial and full EMT to breast cancer malignancy. *Dev. Cell* **56**, 3203–3221 (2021).
8. Pastushenko, I. & Blanpain, C. EMT transition states during tumor progression and metastasis. *Trends Cell Biol.* **29**, 212–226 (2019).
9. Lengrand, J. et al. Pharmacological targeting of netrin-1 inhibits EMT in cancer. *Nature* **620**, 402–408 (2023).
10. Pérez-González, A. et al. Single cell multiomics unravel the transcription networks controlling the different EMT tumor states. *Nat. Commun.* **17**, 8561 (2026).
11. de Visser, K. E. & Joyce, J. A. The evolving tumor microenvironment: from cancer initiation to metastatic outgrowth. *Cancer Cell* **41**, 374–403 (2023).
12. van Vlerken-Ysla, L., Tyurina, Y. Y., Kagan, V. E. & Gabrilovich, D. I. Functional states of myeloid cells in cancer. *Cancer Cell* **41**, 490–504 (2023).
13. Joyce, J. A. & Fearon, D. T. T cell exclusion, immune privilege, and the tumor microenvironment. *Science* **348**, 74–80 (2015).
14. Lavie, D., Ben-Shmuel, A., Erez, N. & Scherz-Shouval, R. Cancer-associated fibroblasts in the single-cell era. *Nat. Cancer* **3**, 793–807 (2022).
15. Kloosterman, D. J. & Akkari, L. Macrophages at the interface of the co-evolving cancer ecosystem. *Cell* **186**, 1627–1651 (2023).
16. Monteran, L., Zait, Y. & Erez, N. It's all about the base: stromal cells are central orchestrators of metastasis. *Trends Cancer* **10**, 208–229 (2024).
17. Malagoli Tagliazucchi, G., Wiecek, A. J., Withnell, E. & Secrier, M. Genomic and microenvironmental heterogeneity shaping epithelial-to-mesenchymal trajectories in cancer. *Nat. Commun.* **14**, 789 (2023).
18. Fantozzi, A. et al. VEGF-mediated angiogenesis links EMT-induced cancer stemness to tumor initiation. *Cancer Res.* **74**, 1566–1575 (2014).
19. Ligorio, M. et al. Stromal microenvironment shapes the intratumoral architecture of pancreatic cancer. *Cell* **178**, 160–175 (2019).
20. Yu, Y. et al. Cancer-associated fibroblasts induce epithelial–mesenchymal transition of breast cancer cells through paracrine TGF-β signalling. *Br. J. Cancer* **110**, 724–732 (2014).
21. Fan, Q.-M. et al. Tumor-associated macrophages promote cancer stem cell-like properties via transforming growth factor-β1-induced epithelial–mesenchymal transition in hepatocellular carcinoma. *Cancer Lett.* **352**, 160–168 (2014).
22. Cohen, E. N. et al. Inflammation mediated metastasis: immune induced epithelial-to-mesenchymal transition in inflammatory breast cancer cells. *PLoS ONE* **10**, e0132710 (2015).
23. Rawal, P. et al. Endothelial cell-derived TGF-β promotes epithelial–mesenchymal transition via CD133 in HBx-infected hepatoma cells. *Front. Oncol.* **9**, 308 (2019).
24. Goulet, C. R. et al. Cancer-associated fibroblasts induce epithelial–mesenchymal transition of bladder cancer cells through paracrine IL-6 signalling. *BMC Cancer* **19**, 137 (2019).
25. Che, D. et al. Macrophages induce EMT to promote invasion of lung cancer cells through the IL-6-mediated COX-2/PGE2/β-catenin signalling pathway. *Mol. Immunol.* **90**, 197–210 (2017).
26. Soon, P. S. H. et al. Breast cancer-associated fibroblasts induce epithelial-to-mesenchymal transition in breast cancer cells. *Endocr. Relat. Cancer* **20**, 1–12 (2013).
27. West, N. R., Murray, J. I. & Watson, P. H. Oncostatin-M promotes phenotypic changes associated with mesenchymal and stem cell-like differentiation in breast cancer. *Oncogene* **33**, 1485–1494 (2014).
28. Smigiel, J. M., Parameswaran, N. & Jackson, M. W. Potent EMT and CSC phenotypes are induced by oncostatin-M in pancreatic cancer. *Mol. Cancer Res.* **15**, 478–488 (2017).
29. Junk, D. J. et al. Oncostatin M promotes cancer cell plasticity through cooperative STAT3–SMAD3 signaling. *Oncogene* **36**, 4001–4013 (2017).
30. Hara, T. et al. Interactions between cancer cells and immune cells drive transitions to mesenchymal-like states in glioblastoma. *Cancer Cell* **39**, 779–792 (2021).
31. Lee, B. Y. et al. Heterocellular OSM–OSMR signalling reprograms fibroblasts to promote pancreatic cancer growth and metastasis. *Nat. Commun.* **12**, 7336 (2021).
32. Tickle, T., Tirosh, I., Georgescu, C., Brown, M. & Haas, B. inferCNV of the Trinity CTAT Project. *Bioconductor* https://github.com/broadinstitute/inferCNV (2019). Q22
33. Zhang, B. et al. Multitranscriptome analysis reveals stromal cells in the papillary dermis to promote angiogenesis in psoriasis vulgaris. *Br. J. Dermatol.* **192**, 672–683 (2025).
34. Lee, S. B. et al. Dickkopf-related protein 2 promotes hair growth by upregulating the Wnt/β-catenin signaling pathway in human dermal papilla cells. *Ann. Dermatol.* **36**, 292–299 (2024).
35. Caronni, N. et al. IL-1β^{+} macrophages fuel pathogenic inflammation in pancreatic cancer. *Nature* **623**, 415–422 (2023).

36. Coffelt, S. B., Wellenstein, M. D. & de Visser, K. E. Neutrophils in cancer: neutral no more. *Nat. Rev. Cancer* **16**, 431–446 (2016).
37. Yu, M. et al. Circulating breast tumor cells exhibit dynamic changes in epithelial and mesenchymal composition. *Science* **339**, 580–584 (2013).
38. Troulé, K. et al. CellPhoneDB v5: inferring cell–cell communication from single-cell multiomics data. *Nat. Protoc.* **20**, 3412–3440 (2025).
39. Jin, S., Plikus, M. V. & Nie, Q. CellChat for systematic analysis of cell–cell communication from single-cell transcriptomics. *Nat. Protoc.* **20**, 180–219 (2025).
40. Batlle, E. et al. The transcription factor Snail is a repressor of E-cadherin gene expression in epithelial tumour cells. *Nat. Cell Biol.* **2**, 84–89 (2000).
41. Hajra, K. M., Chen, D. Y.-S. & Fearon, E. R. The SLUG zinc-finger protein represses E-cadherin in breast cancer. *Cancer Res.* **62**, 1613–1618 (2002).
42. Vesuna, F., van Diest, P., Chen, J. H. & Raman, V. Twist is a transcriptional repressor of E-cadherin gene expression in breast cancer. *Biochem. Biophys. Res. Commun.* **367**, 235–241 (2008).
43. Cano, A. et al. The transcription factor Snail controls epithelial–mesenchymal transitions by repressing E-cadherin expression. *Nat. Cell Biol.* **2**, 76–83 (2000).
44. Liongue, C., Wright, C., Russell, A. P. & Ward, A. C. Granulocyte colony-stimulating factor receptor: stimulating granulopoiesis and much more. *Int. J. Biochem. Cell Biol.* **41**, 2372–2375 (2009).
45. Sawant, K. V. et al. Neutrophil recruitment by chemokines CXCL1/KC and CXCL2/MIP2: role of CXCR2 activation and glycosaminoglycan interactions. *J. Leukoc. Biol.* **109**, 777–791 (2021).
46. Qian, B.-Z. et al. CCL2 recruits inflammatory monocytes to facilitate breast-tumour metastasis. *Nature* **475**, 222–225 (2011).
47. Pyonteck, S. M. et al. CSF-1R inhibition alters macrophage polarization and blocks glioma progression. *Nat. Med.* **19**, 1264–1272 (2013).
48. Qian, D. et al. The dual roles of chemokine (C-C motif) ligand 7 in tumors and inflammatory diseases. *PeerJ* **14**, e20685 (2026).
49. Ishida, Y. et al. Pivotal involvement of the CX3CL1–CX3CR1 axis for the recruitment of M2 tumor-associated macrophages in skin carcinogenesis. *J. Invest. Dermatol.* **140**, 1951–1961 (2020).
50. Xu, J., Lamouille, S. & Derynck, R. TGF-β-induced epithelial to mesenchymal transition. *Cell Res.* **19**, 156–172 (2009).
51. Jones, S. A. & Jenkins, B. J. Recent insights into targeting the IL-6 cytokine family in inflammatory diseases and cancer. *Nat. Rev. Immunol.* **18**, 773–789 (2018).
52. Li, Y. et al. p63: a crucial player in epithelial stemness regulation. *Oncogene* **42**, 3371–3384 (2023).
53. Wang, P.-C. et al. Activation of VCAM-1 and its associated molecule CD44 leads to increased malignant potential of breast cancer cells. *Int. J. Mol. Sci.* **15**, 3560–3579 (2014).
54. McFaline-Figueroa, J. L. et al. A pooled single-cell genetic screen identifies regulatory checkpoints in the continuum of the epithelial-to-mesenchymal transition. *Nat. Genet.* **51**, 1389–1398 (2019).
55. Seguin, L. et al. An integrin β3–KRAS–RALB complex drives tumour stemness and resistance to EGFR inhibition. *Nat. Cell Biol.* **16**, 457–468 (2014).
56. Wainberg, Z. A. et al. Neoadjuvant modified FOLFIRINOX plus nivolumab in borderline-resectable pancreatic ductal adenocarcinoma: a pilot phase 1 trial. *Nat. Commun.* **17**, 2232 (2026).
57. Godin, L. et al. A novel approach for quantifying cancer cells showing hybrid epithelial/mesenchymal states in large series of tissue samples: towards a new prognostic marker. *Cancers* **12**, 906 (2020).
58. Araujo, A. M. et al. Stromal oncostatin M cytokine promotes breast cancer progression by reprogramming the tumor microenvironment. *J. Clin. Invest.* **132**, e148667 (2022).
59. Adrover, J. M. et al. Neutrophils drive vascular occlusion, tumour necrosis and metastasis. *Nature* **645**, 484–495 (2025).
60. Shien, K. et al. JAK1/STAT3 activation through a proinflammatory cytokine pathway leads to resistance to molecularly targeted therapy in non-small cell lung cancer. *Mol. Cancer Ther.* **16**, 2234–2245 (2017).
61. Srinivas, S. et al. Cre reporter strains produced by targeted insertion of *EYFP* and *ECFP*into the *ROSA26*locus. *BMC Dev. Biol.* **1**, 4 (2001).
62. Barker, N. et al. Identification of stem cells in small intestine and colon by marker gene *Lgr5*. *Nature* **449**, 1003–1007 (2007).
63. Tuveson, D. A. et al. Endogenous oncogenic *K-ras*^{G12D} stimulates proliferation and widespread neoplastic and developmental defects. *Cancer Cell* **5**, 375–387 (2004).
64. Jonkers, J. et al. Synergistic tumor suppressor activity of BRCA2 and p53 in a conditional mouse model for breast cancer. *Nat. Genet.* **29**, 418–425 (2001).
65. Lapouge, G. et al. Skin squamous cell carcinoma propagating cells increase with tumour progression and invasiveness. *EMBO J.* **31**, 4563–4575 (2012).
66. Wolf, F. A., Angerer, P. & Theis, F. J. SCANPY: large-scale single-cell gene expression data analysis. *Genome Biol.* **19**, 15 (2018).
67. Young, M. D. & Behjati, S. SoupX removes ambient RNA contamination from droplet-based single-cell RNA sequencing data. *Gigascience* **9**, giaa151 (2020).
68. Germain, P.-L., Lun, A., Meixide, C. G., Macnair, W. & Robinson, M. D. Doublet identification in single-cell sequencing data using scDblFinder. Preprint at *F1000Res.* https://doi.org/10.12688/f1000research.73600.2 (2022).
69. Zappia, L. & Oshlack, A. Clustering trees: a visualization for evaluating clusterings at multiple resolutions. *Gigascience* **7**, giy083 (2018).
70. Franzén, O., Gan, L.-M. & Björkegren, J. L. M. PanglaoDB: a web server for exploration of mouse and human single-cell RNA sequencing data. *Database* **2019**, baz046 (2019).
71. Lopez, R., Regier, J., Cole, M. B., Jordan, M. I. & Yosef, N. Deep generative modeling for single-cell transcriptomics. *Nat. Methods* **15**, 1053–1058 (2018).
72. Korsunsky, I. et al. Fast, sensitive and accurate integration of single-cell data with Harmony. *Nat. Methods* **16**, 1289–1296 (2019).
73. Dimitrov, D. et al. LIANA+ provides an all-in-one framework for cell–cell communication inference. *Nat. Cell Biol.* **26**, 1613–1622 (2024).
74. Palla, G. et al. Squidpy: a scalable framework for spatial omics analysis. *Nat. Methods* **19**, 171–178 (2022).
75. Dai, M. et al. LARIS enables accurate and efficient ligand and receptor interaction analysis in spatial transcriptomics. Preprint at *bioRxiv* https://doi.org/10.1101/2025.11.26.690796 (2025).
76. Subramanian, A. et al. Gene set enrichment analysis: a knowledge-based approach for interpreting genome-wide expression profiles. *Proc. Natl Acad. Sci. USA* **102**, 15545–15550 (2005).
77. Badia-i-Mompel, P. et al. decoupleR: ensemble of computational methods to infer biological activities from omics data. *Bioinform. Adv.* **2**, vbac016 (2022).

Acknowledgements

We thank the Université Libre de Bruxelles (ULB) animal facility, ULB genomic core facility (F. Libert, A. Lefort and S. Paternot) for bulk RNA-seq and scRNA-seq, A. Bauduin for help with 10x Xenium analysis, D. Engelman for help with microscopy imaging and J. Zuber for the CRISPR–Cas9 plasmids.

Author contributions

A.D., S.V. and C.B. designed the experiments and performed the analysis. A.D. performed the biological experiments. S.V. performed the bioinformatic analysis. A.P.G. and K.B. generated scRNA-seq datasets; A.P.G. also helped in the generation of spatial transcriptomic datasets. K.B. also contributed to cell culture experiments by generating the Cas9-infected cell line. L.V.d.P. and Z.Z. helped with follow-up of the mice, cell culture, western blots, immunostaining and PCRs. S.R. and I.S. provided human urothelial cancer samples. J.A. performed the immunofluorescence and immunohistochemistry staining on human urothelial tumors. C.D. helped to perform FACS. All authors read and approved the final manuscript.

Funding

A.D. is supported by an EMBO long-term fellowship (ALTF-665-2022) and FNRS postdoctoral researcher fellowship; S.V. is supported by FNRS–FWO EOS (40007513) and TELEVIE (7.4513.24); A.P.G. is supported by the ITN network EVOMET (955951) of the EU Horizon 2020 research; K.B. is supported by TELEVIE; and C.B. is supported by WEL Research Institute, FNRS, TELEVIE, Fonds Erasme, Fondation Contre le Cancer, the ULB Foundation, FNRS–FWO EOS (40007513) and European Research Council advanced grant TTTS (AdvGrant 885093). The funders had no role in study design, data collection and analysis, decision to publish or preparation of the manuscript.

Competing interests

C.B. reports ownership of shares in Cancer State Therapeutics. The authors declare that this project is unrelated to the company's activities and that no conflict of interest exists. The remaining authors declare no competing interests.

Additional information

Extended data is available for this paper at https://doi.org/10.1038/s43018-026-01259-3.

Supplementary information The online version contains supplementary material available at https://doi.org/10.1038/s43018-026-01259-3.

Correspondence and requests for materials should be addressed to Cédric Blanpain.

Peer review information *Nature Cancer* thanks Charles Bidgood, Jean Thiery, Erik Thompson and the other, anonymous, reviewer(s) for their contribution to the peer review of this work. Peer reviewer reports are available.

Reprints and permissions information is available at www.nature.com/reprints.

Publisher's note Springer Nature remains neutral with regard to jurisdictional claims in published maps and institutional affiliations.

Springer Nature or its licensor (e.g. a society or other partner) holds exclusive rights to this article under a publishing agreement with the author(s) or other rightsholder(s); author self-archiving of the accepted manuscript version of this article is solely governed by the terms of such publishing agreement and applicable law.

© The Author(s), under exclusive licence to Springer Nature America, Inc. 2026